fluids

MDPI

Article

Features of Motion and Heat Transfer of Swirling Flows in Channels of Complex Geometry

Sergey Dmitriev [1], Alexey Sobornov [1] and Andrey Kurkin [2,*]

[1] Department of Atomic and Thermal Stations, Nizhny Novgorod State Technical University n.a. R.E. Alekseev, Nizhny Novgorod 603155, Russia; dmitriev@nntu.ru (S.D.); wisestjedi@gmail.com (A.S.)
[2] Department of Applied Mathematics, Nizhny Novgorod State Technical University n.a. R.E. Alekseev, Nizhny Novgorod 603155, Russia
* Correspondence: aakurkin@nntu.ru

Abstract: The computational and experimental study results of swirling single-phase coolant motion and heat transfer for the standard operation parameters of a nuclear power plant are presented. The experimental model is a vertical heat exchanger of a "pipe in a pipe" type with the countercurrent movement of coolants. Six different swirlers (three with a constant twist pitch and three with a variable pitch) were considered. The heat exchanger temperature field was measured at various combinations of coolant flow rates, and a channel pressure drop for each swirl was determined. Computational studies were performed using the Omega-based Reynolds stress model and SST model with a correction for curvature streamlines. A good agreement between numerical and experimental data was obtained. Based on the velocity and temperature fields, swirling flow motion features in channels with a variable swirl pitch were discovered. For each intensifier, the effectiveness criterion in comparison with a pipe channel was determined.

Keywords: swirling flow; heat transfer intensification; hydrodynamics; PWR heat exchangers; computational fluid dynamics; Omega Reynolds stress model

check for updates

Citation: Dmitriev, S.; Sobornov, A.; Kurkin, A. Features of Motion and Heat Transfer of Swirling Flows in Channels of Complex Geometry. *Fluids* **2024**, *9*, 293. https://doi.org/10.3390/fluids9120293

Academic Editors: Kamil Urbanowicz and Tomoaki Kunugi

Received: 18 September 2024
Revised: 20 November 2024
Accepted: 27 November 2024
Published: 10 December 2024

Copyright: © 2024 by the authors. Licensee MDPI, Basel, Switzerland. This article is an open access article distributed under the terms and conditions of the Creative Commons Attribution (CC BY) license (https://creativecommons.org/licenses/by/4.0/).

1. Introduction

To reach the highest level of modern nuclear power engineering, the energy efficiency of heat exchanger equipment needs to be increased. The most rational way to solve this problem, together with avoiding a significant increase in the heat exchange equipment's weight and size, is the intensification of heat and mass transfer processes.

The intensification methods of convective heat exchange can be of two types: active and passive [1]. The active methods require additional energy costs (mechanical, electromagnetic, etc.) to affect the heat exchange mechanism. The energy transfer to a fluid flow during active intensification can be carried out by various means: rotation and vibration of the heat exchange surface, vibration of the coolant, injection, or suction of the coolant through a porous surface, and imposition of electrostatic or electromagnetic fields. However, the active methods listed above are either technically difficult to implement or energetically inefficient, and as a result, they do not find practical application in heat exchangers of power plants. Passive methods of heat exchange intensification are widely used in NPU units [2]. Their action is aimed at turbulization or destruction of the boundary layer, turbulization of the entire fluid flow, as well as an increase in the heat exchange surface, especially from the side where the heat exchange intensity is too low.

One of the effective passive ways to increase energy efficiency is to create curved heat exchange surfaces, leading to a swirl of the coolant flow [3–5]. The flow's swirling can also be carried out in straight-tube bundles with their inherent high compactness, using various types of screw inserts. These inserts can be belt and blade swirlers or screw inserts made by cutting or winding wire onto a rod. A special place among the passive methods of heat exchange intensification is occupied by tape flow swirlers [6]. They, as

well as auger swirlers, make it possible to increase heat transfer intensity due to secondary flows arising under the action of centrifugal forces, which intensify heat exchange between the core of the flow and the boundary layer. Tape swirlers are the simplest ones and are not expensive to manufacture compared to other methods of intensification [7–9]. The channels with tape swirlers have less pressure drop compared to auger turbulators with the same heat transfer coefficient. This intensification method is characterized by lower metal consumption. This intensification method can be used to modernize heat exchangers [10]. In this case, there is no need to design a new heat exchanger; it is enough to insert a twisted tape into the heat exchange channel. The most acceptable intensifier geometry is selected by varying the winding step or using a variable step. An important drawback of any heat transfer intensification method is the additional pressure drop that arises. Regardless of intensification aims and conditions, the pressure drop of the improved channel must be evaluated. The efficiency assessment result is based on a combination of coefficients that take into account changes in the heat exchange surface area and heat flow and the increase in channel pressure drop.

In nuclear reactors, like the PWR or WWER, the heat exchange equipment functions within unique operation parameters. The most important of these is the high-temperature field gradient. The temperature field change along the length of the channel leads to significant changes in the physical properties of the coolant. For example, at 10 MPa of pressure, if the temperature changes from 35 to 200 degrees, the dynamic viscosity decreases by 5.2 times, the kinematic viscosity by 6.3 times, and the Prandtl number by 5.3 times [11]. The generalized dependencies $Nu = f\ (Re, Pr)$, which are experimentally obtained within a narrow range of parameter changes, can be used in the heat exchange surface design very carefully.

It will be more accurate to use modern CFD codes, which will make it easy to take into account all factors. At the moment, there is a wide variety of CFD codes. Most of them are based on the Navier–Stokes equation's solution for coolant turbulent flow. Since the direct solution (DNS) of a system of equations requires high-performance computer systems, turbulence models have become the most widespread. These are additional equations to the system, the main aim of which is to simplify and speed up equation solving. The most popular among them are RANS (k-e, k-ω, and SST), DES and LES models. All turbulent models are based on additional experimental studies. They need to be carried out for various coefficient adjustments, making it possible to improve the quality of the resulting solution despite the introduced simplifications.

In this study, the authors try to evaluate the application of Omega-based Reynolds stress (ORS) [12] and SST-CC [13,14] with a correction for curvature streamline models of turbulence for coolant flow modeling, moving in the swirling channel with large temperature changes. Numerical modeling was carried out by Ansys CFX. Numerical approaches' validation was carried out by an experimental study of heat transfer within PWR operation parameters [15–17]. The high level of numerical details made it possible to identify some swirling flow features that occur when the twist pitch changes.

2. Swirl Flow Study Overview

In the context of the physical processes considered in this article, the theoretical and experimental studies of single-phase coolant swirling flows are of main interest. Extensive studies in this field were conducted by Koch [18], Shchukin [19], R.M. Manglik and A.E. Bergles [20], and others [21,22]. The main geometric characteristics of a channel with an inserted twisted tape are the diameter (d), tape thickness (δ), and swirl pitch (s), corresponding to a 180° turn of the flow around the pipe axis (Figure 1).

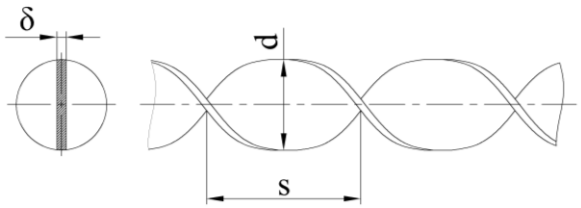


Figure 1. Twisted tape configuration.

The flow swirl intensity can be assessed in several ways as follows:

- The relative pitch of the helical line, where *s/d* is a simple and less effective parameter;
- The max swirl angle (θ), which is the local parameter of the limiting streamline deviation from the axial direction [19]:

$$\tan(\theta) = \frac{\tau_\varphi}{\tau_z}, \quad (1)$$

where τ_φ, τ_z is the tangential stress projections onto the angular and axial directions;

- The integral twist parameter (Sn) takes into account the velocity uneven distribution in the radial (r) direction as follows:

$$Sn = \frac{\int_0^R \rho u_\Phi u_z r^2 dr}{R\int_0^R \rho u_z^2 r dr}, \quad (2)$$

where u_φ and u_z are the velocity projections onto the angular and axial directions, ρ is the density, and R is the tube channel cross-section radius. This parameter characterizes the relative magnitude of momentum flows transferred in the angular and axial directions [23]. Sn accurate calculation is difficult. In article [24], the authors show that the Sn value has high sensitivity due to the method and limits of integration.

Researchers from [19,23] have found a strong connection between the integral and local swirl parameters, for example, for axial-vane swirlers:

$$\tan(\theta) = 1.13 \cdot Sn^{0.82}, \quad (3)$$

Starting from a threshold value of integral twist parameter Sn^*, ($0.23 < Sn^* < 0.3$) [23], the tangential velocity distribution takes the form as seen in Figure 2.

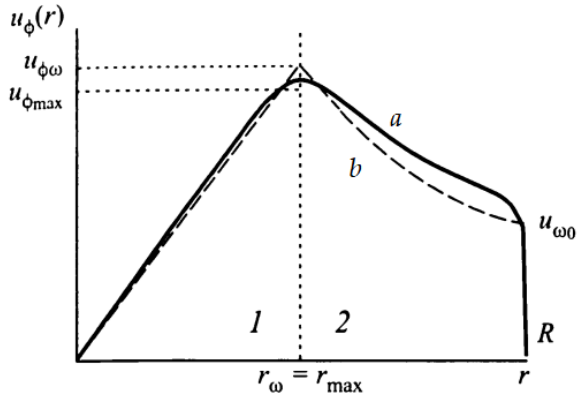


Figure 2. Tangential velocity distribution when $Sn > Sn^*$: (a)—real profile; (b)—theoretical; 1—zone of quasi-rigid rotation; 2—zone of quasi-potential flow.

The theoretical profile calculated by Formula (4):

$$u_{\phi}(r) = \begin{cases} \omega \cdot r \text{ if } 0 < r < r_{\omega}, \\ \frac{u_{\phi\omega} r_{\omega}}{r} \text{ if } r_{\omega} < r < R, \end{cases} \quad (4)$$

where ω is the angular velocity in a quasi-rigid rotation region, r_{ω} is the radius corresponding to the tangential velocity maximum $u_{\varphi\omega}$. At $Sn < Sn^*$, the tangential velocity maximum is achieved near the wall region but outside the viscous sublayer. Regions with positive and negative gauge pressure appear at $Sn > Sn^*$. Swirl attenuation during the rotation degeneration process leads to pressure profile equalization, i.e., to the pressure increasing in the central region. The negative axial pressure gradient leads to reverse flow emergence.

During the coolant movement along a swirling channel, inertial force excess action leads to secondary flows' formation. The laser Doppler anemometry (LDA) method application in the experimental studies and the direct numerical modeling (DNS) method for numerical ones allowed for more accurate localization of stable vortex structures [25]. Two spiral rotating vortices arise in the water flow at room temperature after passing a short swirl insert. Computational and experimental velocity fields refuted the hypothesis of vortices' counter-rotation. Figure 3 shows the evolution of velocity vector distribution at s/d = 2.36 and Re = 77,000. The authors showed that single-rotating vortices were formed on each side of the insert as a result of pressure imbalance that occurs near the inlet region of the twisted tape.

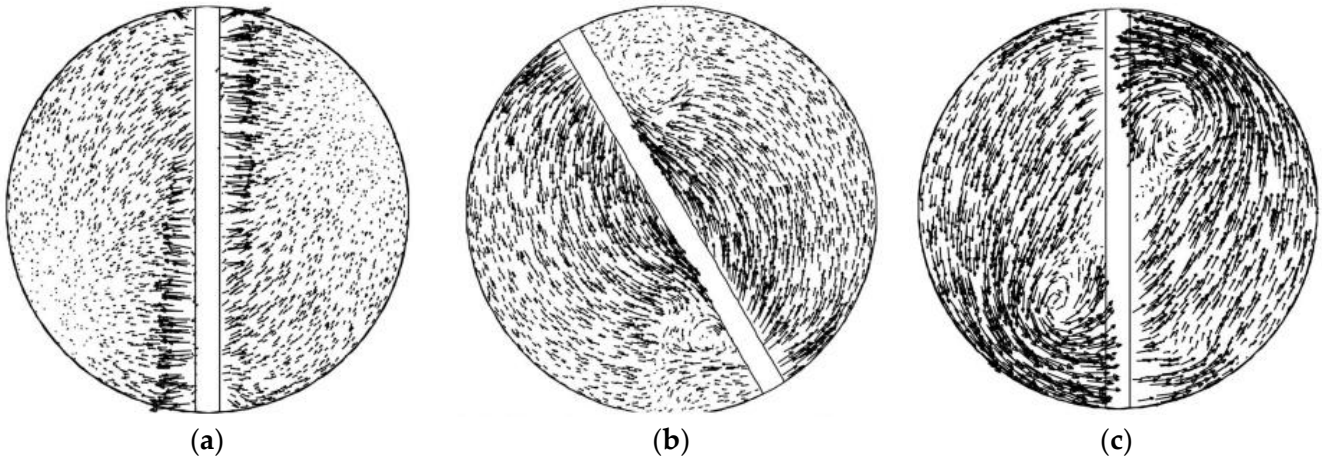


Figure 3. Velocity distribution across the channel cross-section with a tape insert at the inlet (**a**), with flow turning by 75° (**b**) and 180° (**c**).

Some experimental generalized dependencies for heat transfer coefficients and hydraulic friction are presented below. According to Koch R. [18]:

$$\lambda = \frac{6.34}{Re^{0.474}} \left(0.5 + \frac{8}{\pi^2} \left(\frac{s}{d}\right)^2\right)^{-0.263} + \frac{25.6}{Re}, \quad (5)$$

$$Nu = 0.3 Re^{0.6} Pr_f^{0.43} \left(0.5 + \frac{8}{\pi^2} \left(\frac{s}{d}\right)^2\right)^{-0.135}, \text{ if} \quad (6)$$

$$Re_I^{crit} = 11.6 \sqrt{0.5 + \frac{8}{\pi^2} \left(\frac{s}{d}\right)^2} < Re < Re_{II}^{crit} = 38900 \left(\frac{s}{d}\right)^{-1.16} + 2300. \quad (7)$$

According to R.M. Manglik and A.E. Bergles [20], for laminar flow:

$$\lambda = \frac{15.767}{Re} \left[\frac{\pi d + 2d - 2\delta}{\pi d - 4\delta}\right]^2 \left(1 + 10^{-6} Sw^{2.55}\right)^{\frac{1}{6}} \left[\frac{\pi d}{\pi d - 4\delta}\right] \left[1 + \left(\frac{\pi d}{2s}\right)^2\right], \quad (8)$$

$$Nu = 4.612\left(\frac{\mu_f}{\mu_w}\right)^{0.14}\left(\left[\left(1+0.0951Gz^{0.894}\right)^{2.5}+6.413\cdot10^{-9}\left(Sw\cdot Pr^{0.391}\right)^{3.835}\right]^2 +2.132\cdot10^{-14}(Re\cdot Ra)^{2.23}\right)^{0.1}, \quad (9)$$

$$Sw = \frac{Re}{\sqrt{s/d}}\left[\frac{\pi d}{\pi d-4\delta}\right]\sqrt{1+\left(\frac{\pi d}{2s}\right)^2}; \quad (10)$$

and for liquid turbulent flow in a heated channel:

$$\lambda = \frac{0.0791}{Re^{0.25}}\left[1+\frac{2.752}{(s/d)^{1.29}}\right]\left[\frac{\pi d}{\pi d-4\delta}\right]^{1.75}\left[\frac{\pi d+2d-2\delta}{\pi d-4\delta}\right]^{1.25}, \quad (11)$$

$$Nu = 0.023Re^{0.8}Pr^{0.4}\left[1+\frac{0.769}{s/d}\right]\left[\frac{\pi d}{\pi d-4\delta}\right]^{0.8}\left[\frac{\pi d+2d-2\delta}{\pi d-4\delta}\right]^{0.2}\left(\frac{\mu_f}{\mu_w}\right)^{0.18}, \quad (12)$$

where *Re*, *Gz*, *Pr*, *Nu*, and *Ra* are the Reynolds, Graetz, Prandtl, Nusselt, and Rayleigh numbers, λ is the friction coefficient, and μ_f and μ_w are the dynamic viscosity of coolant at the fluid flow center and wall temperature.

3. Experimental Study

This big study was conducted in two stages: experimental and numerical. The experimental study of heat transfer intensification was carried out on the "FT-80" testing branch, which was created to study hydrodynamic and heat transfer processes in steam-generating systems. The test branch includes three hydraulic circuits. The first and the second circuits, filled with bi-distilled water, are hydraulically closed and used under excess pressure, and the third circuit is hydraulically open and made for cooling main equipment. The ranges of operating parameters are as follows:

- Pressure of the first and the second circuits: P_1 = 8 ÷ 11 MPa, P_2 = 3 ÷ 5 MPa;
- Inlet temperature of the first and the second circuits: T_1 = 245 ÷ 260 °C, T_2 = 30 ÷ 50 °C;
- Mass flow rate of the first and the second circuits: G_1 = 11 ÷ 277 kg/h, G_2 = 4 ÷ 114 kg/h;
- Reynolds numbers for the input sections: Re_1 = 1250 ÷ 31,600, Re_2 = 140 ÷ 3900.

The main aim of the experimental study was to obtain the temperature field and pressure drop of the swirling coolant flow in the heat exchanger channel. The general view of the experimental model is shown in Figure 4a, and the schematic view of the interior space is shown in Figure 4b. The model is a heat exchanger channel made according to the "pipe in pipe" principle. The case of the model consists of two parts, which are after welding, and the longitudinal welds form a circular cross-section channel with a 17 mm inner diameter. A heat exchange tube with a 13 mm outer diameter and 1.5 mm wall thickness, made of titanium alloy, is placed along the channel axis (Figure 4c).

The intensifier is a strip made of 12Cr18Ni10Ti stainless steel 1 mm thick and 9.8 mm wide, twisted around the central axis (Figure 5).

The length of the heat exchanger intensifier is equal to the active part length of the experimental model and is equal to 2280 mm. Six metallic bands were manufactured and studied: three with constant twist pitches (s = 20, 30, and 40 mm) and three with a variable twist pitch created on the basis of different combinations of these fragments.

The countercurrent flow of the coolants is organized in the model. The second circuit coolant moves upwards along the inner tube and is heated by the first circuit coolant that moves from the top down in the annular gap. Such a coolants' movement scheme is the most optimal because it allows them to achieve the maximum temperature gradient value with minimum impact of thermal driving head forces on the heat transfer process and coolants' movement. The heat exchange surface's active part length is 2440 mm. The channel total length in which thermocouples are installed is 2280 mm.

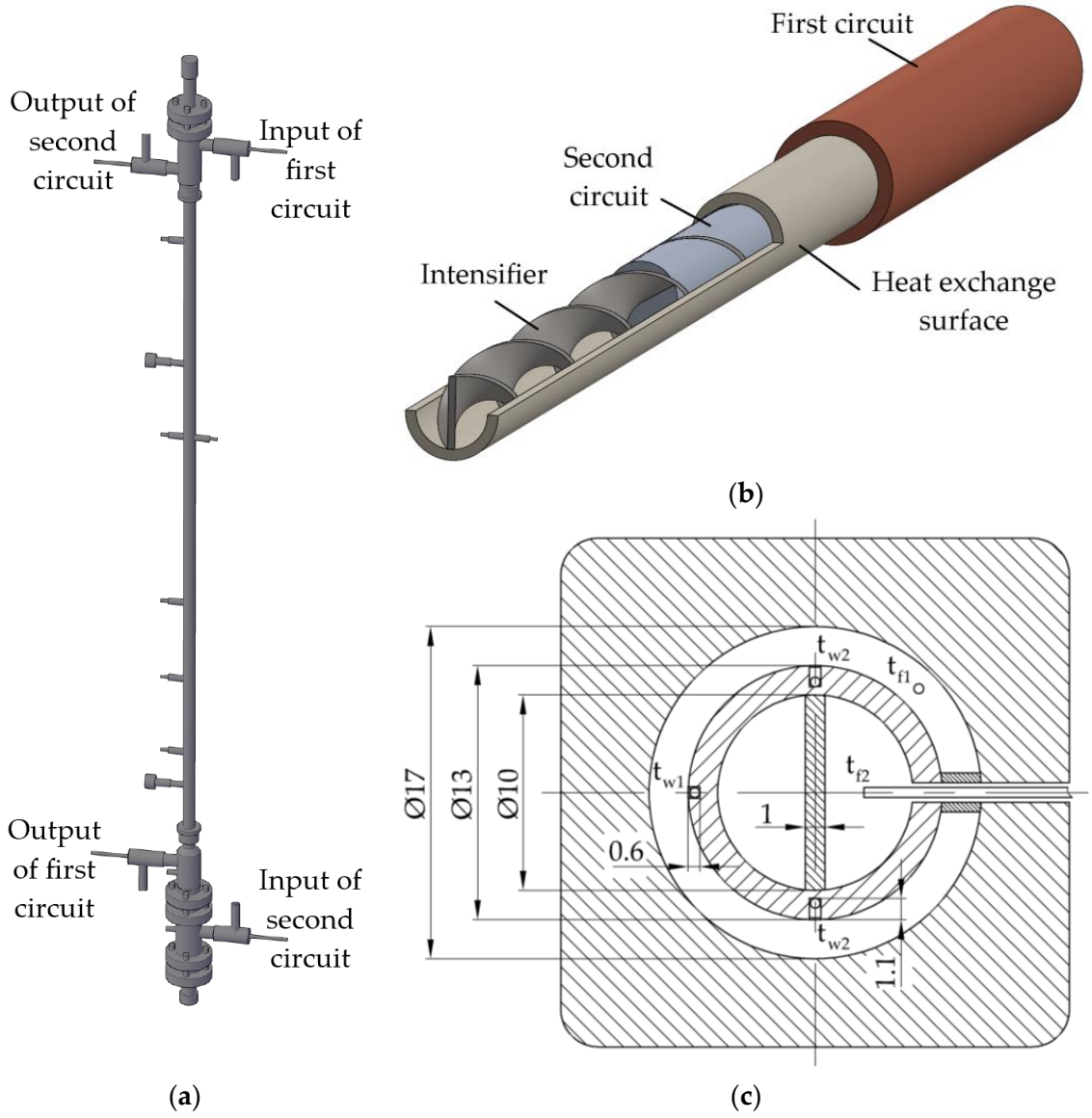


Figure 4. The experimental model: (**a**) general view; (**b**) schematic view of the interior space; (**c**) temperature measurement control points in the section of the model.

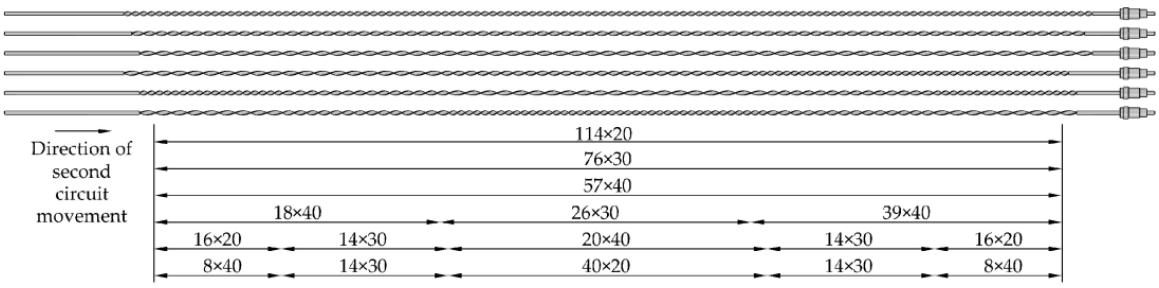


Figure 5. Schematic view of the intensifiers.

Operating parameters and geometric dimensions of the heat exchange surface are selected in such a way as to ensure heat transfer, improving the possibility for swirling heated water: $\alpha_I > \alpha_{II}$. For the specified range of coolants parameters, the heat transfer coefficients' average values, calculated using formulas applicable to annular (13) and round (14), (15) [26] channels, are: α_I = 3400 ÷ 45,000 W/(m^2 ·K), α_{II} = 330 ÷ 5300 W/(m^2·K).

With a significant difference in flow rates, which may occur during the actual operation of heat exchange equipment, a high level of intensification was not achieved along the entire channel length (discussed below).

$$Nu = 0.017Re^{0.8}Pr^{0.4}\left(\frac{Pr_f}{Pr_w}\right)^{0.25}\left(\frac{d_{out}}{d_{in}}\right)^{0.18} \text{ if } Re > 2300, \quad (13)$$

$$Nu = 0.015Re^{0.8}Pr_f^{0.43}\left(\frac{\mu_f}{\mu_w}\right)^{0.14} \text{ if } Re > 2300, \quad (14)$$

$$Nu \cong 3.66 \text{ if } Re < 2300. \quad (15)$$

The temperature of the coolants and the heat exchange surface is measured in 11 sections along the height of the model. These sections include a different set of thermocouples. In the general case, there are:

- Two sets (2 × 11 units) of thermocouples (T_{W2a}, T_{W2b}) embedded to 1.1 mm depth inside the heat exchange surface, designed to measure the wall temperature from the heated coolant side;
- Four at a 0.6 mm depth to measure the wall temperature from the heating coolant side (T_{W1});
- Eight to measure the heating coolant temperature (T_{F1});
- Five temperature sensors for the heated coolant (T_{F2}).

The temperature sensors' active part is located in the central part of the flow. The thermocouples T_{W1} and T_{W2} metallization were performed by plasma spraying in an inert gas (argon) flow. The applied coatings are treated flush with the main surface. All thermocouples (type K) have individual calibration, so the maximum temperature measurement error was 0.5 °C. The maximum value of the heat loss does not exceed 0.5%. Such small heat loss values allow us to exclude them from further numerical analysis.

The channel pressure drop was measured at the heat exchange process when present and absent. At states with $T \neq$ const, the pressure drop is measured by the differential pressure sensor, Yokogawa EJX110A. The maximum relative measurement error value was 0.5%. A significant contribution to the pressure drop measurement error was made by the back pressure of the water column in the measuring tubes connected to the measuring device located at the bottom of the model. For this reason, additional studies were conducted on channel pressure drop with a horizontal model arrangement (Figure 6).

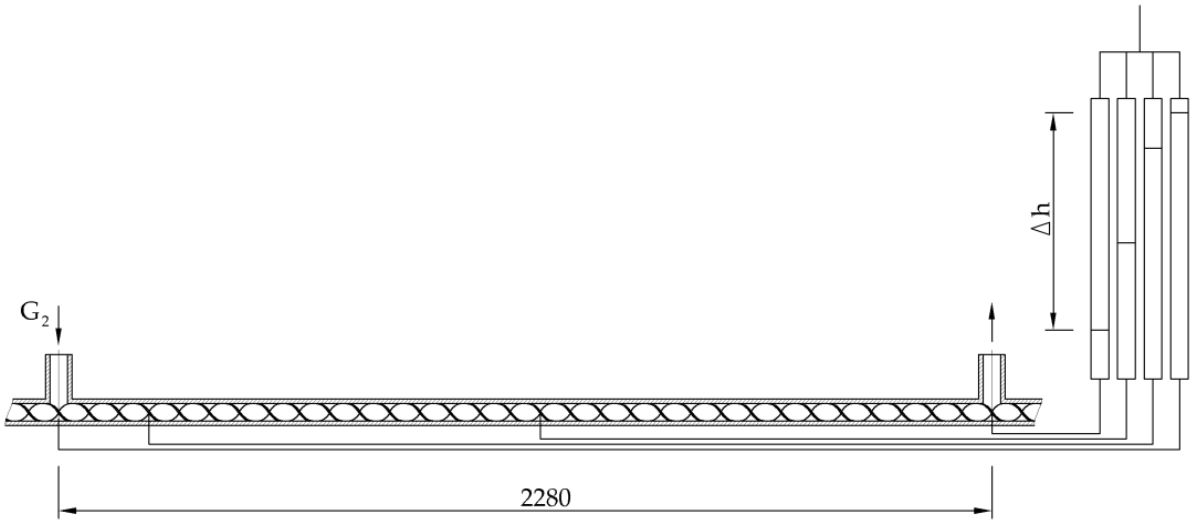


Figure 6. The isothermal flow pressure drop measuring.

Using an isothermal formulation (T = 20 °C), it was possible to significantly increase the measurement accuracy (0.5 mm of water column or ΔP = 5 Pa) by connecting piezometers to the fittings of temperature sensors. More information about the experimental studies can be obtained from [15–17].

4. Experimental Data Processing

From the point of view of thermal process modeling in heated channels, the heat transfer coefficient distribution along the model length has the greatest representation. A computational and experimental distribution comparative analysis makes it possible to evaluate the effectiveness of using a variable twist step. The characteristic temperature distribution in Figure 7 shows that the initial set of thermocouples does not allow for control of the heated coolant temperature in each section of the experimental model. In the first step, the T_{F2} measured values were approximated by different functions in order to determine the missing values.

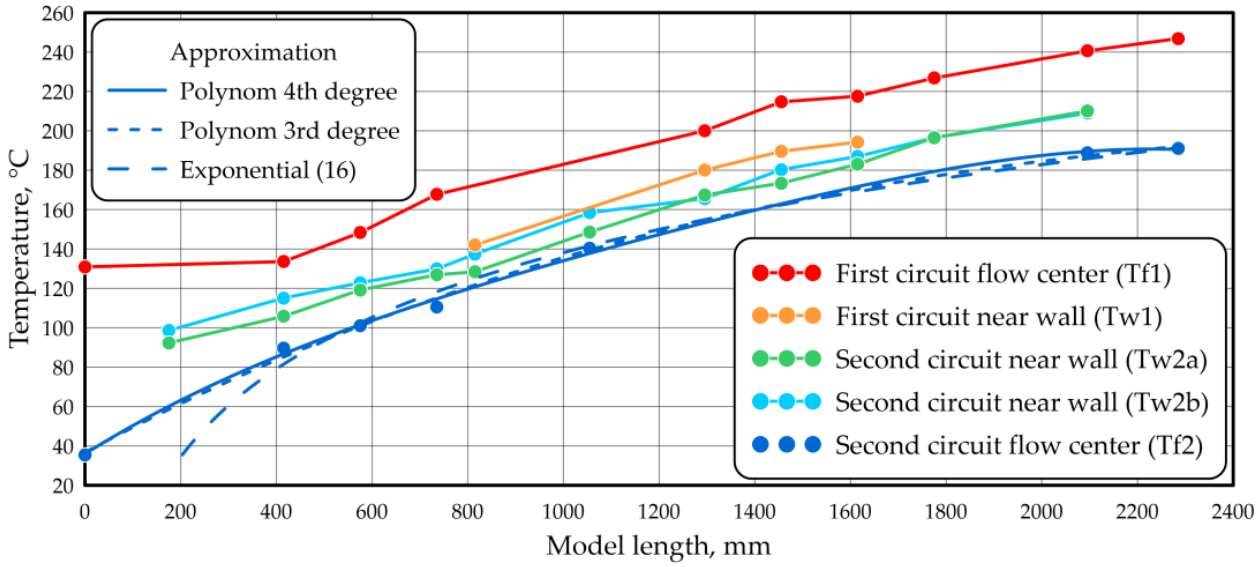


Figure 7. An example of temperature distribution.

The classical analytical solution for the heat exchanger temperature field with the coolants' counter-movement gives a function for heated coolant temperature $T_2(x)$ [27]:

$$T_2(x) = Ae^{Bx} + C, A, B, C - \text{const.} \quad (16)$$

This type of approximation has several disadvantages: firstly, it is obtained with the film coefficient constant value along the length, which is not observed in the experiment; secondly, it does not have significant flexibility and provides rough approximations to the true values. Polynomial functions are simpler and are also suitable for modes with significant differences in flow rates. The optimal polynomial degree is determined from the condition of the minimum value of the sum of deviations from the experimental values (least squares). The application of higher-order polynomials provides non-physical results. Table 1 contains values of least squares sums for different orders of polynomials, shown in Figure 7. As a result, a fourth-degree polynomial was chosen for all experimental modes.

Table 1. Residual sum of squares for approximation polynomials.

Type of Swirlers	Residual Sum of Squares	Type of Swirlers	Residual Sum of Squares
1st degree	992.41	3rd degree	47.02
2nd degree	50.63	4th degree	33.12

To obtain heat transfer coefficient distribution, the heat exchange surface was divided into 10 fragments based on the vertical coordinate of 11 measuring sections. There are two sets of T_{W2} thermocouples as well as a significant uncertainty of their position relative to the installed tape, and their values were averaged over the cross-section. In the next step, the following parameters were determined for each fragment:

- Average (t_f) and boundary values of the flow temperature (t_{in} and t_{out}) and average wall temperature (t_w);
- The heat flow to heated coolant (Q) was determined based on the mass flow rate (G_2) and the enthalpy difference (h_{in} and h_{out}):

$$Q = G_2(h_{out} - h_{in}); \quad (17)$$

- Using the fragment length (l), channel diameter (d), and intensifier thickness (δ), the heat transfer area (S_T) and heat transfer coefficient (α_e) were determined as follows:

$$S_T = (\pi d - 2\delta)l; \quad (18)$$

$$\alpha_e = \frac{Q}{S_T(t_F - t_W)}. \quad (19)$$

5. Numerical Study

The following two-stage numerical approach was used:

- Isothermal swirling-flow modeling was conducted on a lightweight mesh model to obtain velocity and pressure fields using the SST and ORS turbulence models. Also, at this stage, the selection of RANS turbulence models was carried out, which showed the highest accuracy of the solution. These results are not included in this article;
- Heat transfer process simulation was conducted in cases of oncoming movement of coolants using selected turbulence models. For the heating coolant, the SST turbulence model was used in all calculations.

The computational models presented in Figure 8 are geometrical copies of the experimental model. Two mesh models for each intensifier were made as follows:

- Full model—for heat transfer modeling with coolant counterflows—50 million elements (Figure 8a);
- Lightweight model—for isothermal modeling of only one heated flow—12 million elements (Figure 8b).

When creating the analysis area, the following assumptions were made:

- The manifolds necessary for sealing flows' input and output have been discarded;
- Flow rotation presence at 90°, the complex manifold's interior geometry, and a small distance between the entry point and the first measuring section made it possible to consider the heated flow structure on the inlet as uniform: *V(x,y,z) = const*;
- The model created is more streamlined: the faces and other geometrical shape inaccuracies are not taken into account because it would significantly increase the dimensionality of the task and require more computational resources and time for modeling;
- Thermal losses are not taken into account: when specifying boundary conditions, we assume that there is no thermal flow on the outer wall.

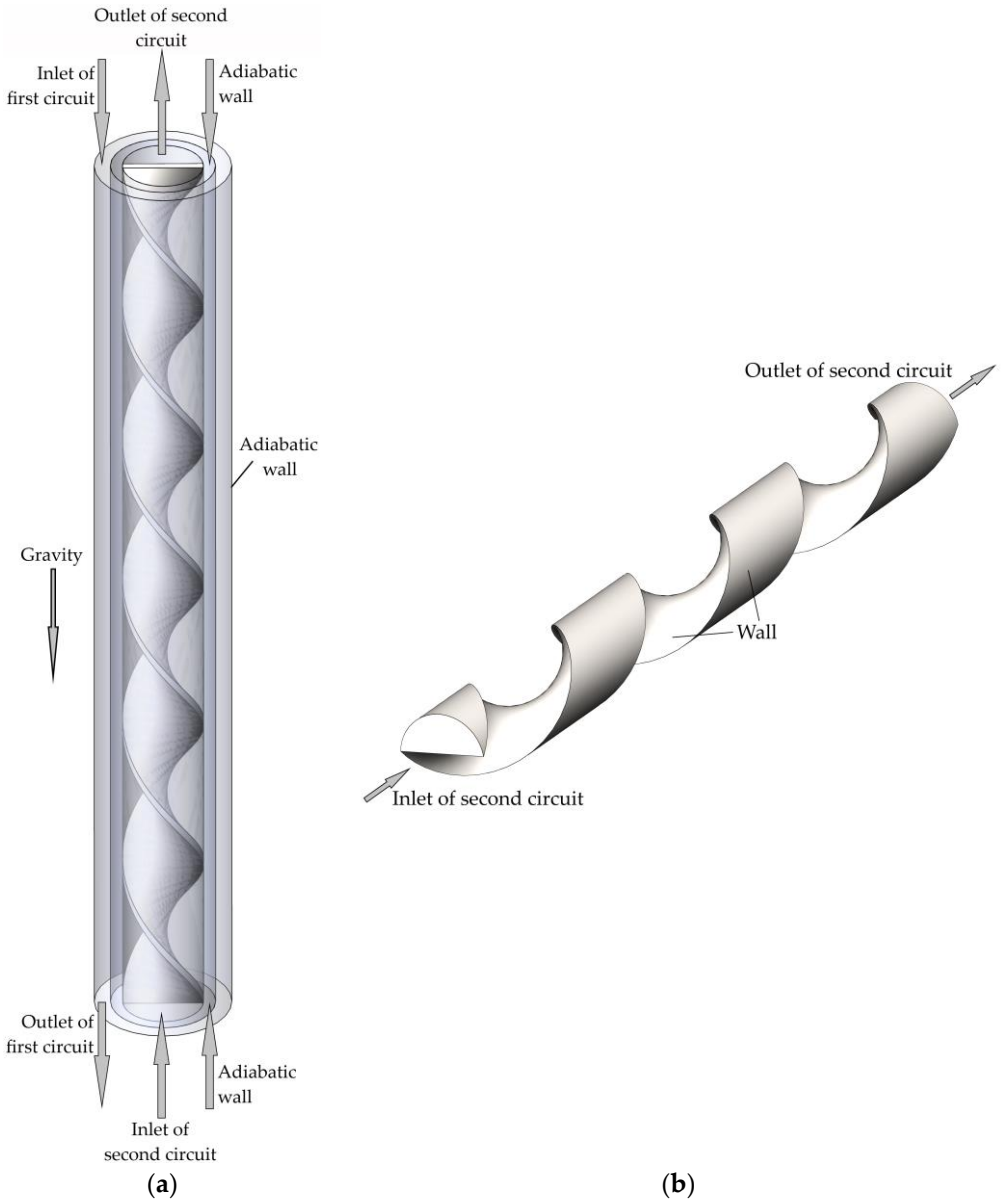


Figure 8. Numerical models: (**a**) schematic view of a full-scale model; (**b**) schematic view of a lightweight model.

Mathematically, the problem's solution is based on solving the basic system of continuity (20), momentum (21) and (22), energy transfer for fluids (23) and (24), and for solids (25) equations:

$$\frac{\partial \rho}{\partial t} + \nabla \cdot \left(\rho \vec{U}\right) = 0, \tag{20}$$

$$\frac{\partial}{\partial t}\left(\rho \vec{U}\right) + \nabla \cdot \left(\rho \vec{U} \otimes \vec{U}\right) = -\nabla P + \nabla \cdot \tau + \left(\rho - \rho_{ref}\right)\vec{g}, \tag{21}$$

$$\tau = \mu\left(\nabla \vec{U} + \left(\nabla \vec{U}\right)^T - \frac{2}{3}\delta \nabla \cdot \vec{U}\right), \tag{22}$$

$$\frac{\partial}{\partial t}\left(\rho\left(E + \frac{U^2}{2}\right)\right) + \nabla \cdot \left(\rho \vec{U}\left(h + \frac{U^2}{2}\right)\right) = \nabla \cdot \left(\left(\lambda + \frac{\mu_t}{\mathrm{Pr}_t} C_P\right)\nabla T\right), \tag{23}$$

$$h = \int_{298.15}^{T} C_P dT + \frac{P}{\rho}, E = h - \frac{P_{OP} + P}{\rho}, \tag{24}$$

$$\frac{\partial}{\partial t}\left(\rho \int_{298.15}^{T} C_p dT\right) = \nabla \cdot (\lambda \nabla T), \tag{25}$$

where μ, λ, and C_P are the dynamic viscosity, thermal conductivity, and heat capacity of the material, respectively, U is the fluid velocity, ρ_{ref} is the density in reference point, τ is the stress tensor, δ (or δ_{ij}) is the Kronecker delta, μ_t is the turbulent viscosity, Pr_t = 1.1 is the turbulent Prandtl number for water [28], E and h are the fluid internal energy and enthalpy, and P and P_{OP} are the gauge and operating pressure.

The use of the SST-CC [12–14] turbulence model implies the solution of two additional transport equations: turbulence kinetic energy (k) (26) and the rate of dissipation of eddies (ω) (27):

$$\frac{\partial(\rho k)}{\partial t} + \frac{\partial(\rho U_j k)}{\partial x_j} = P_k - 0.09\rho\omega k + \frac{\partial}{\partial x_j}\left(\left(\mu + \frac{\mu_t}{\sigma_k}\right)\frac{\partial k}{\partial x_j}\right), \tag{26}$$

$$\frac{\partial(\rho\omega)}{\partial t} + \frac{\partial(\rho U_j \omega)}{\partial x_j} = \alpha\frac{\rho\omega}{k}P_k - \beta\rho\omega^2 + \frac{\partial}{\partial x_j}\left(\left(\mu + \frac{\mu_t}{\sigma_\omega}\right)\frac{\partial\omega}{\partial x_j}\right) + 1.712(1 - F_1)\frac{\rho}{\omega}\frac{\partial k}{\partial x_j}\frac{\partial\omega}{\partial x_j}, \tag{27}$$

$$P_k = f_r\left(\mu_t\left(\frac{\partial U_i}{\partial x_j} + \frac{\partial U_j}{\partial x_i}\right)\frac{\partial U_i}{\partial x_j} - \frac{2}{3}\frac{\partial U_k}{\partial x_k}\left(3\mu_t\frac{\partial U_k}{\partial x_k} + \rho k\right)\right), \tag{28}$$

$$\mu_t = \frac{0.31\rho k}{\max(0.31\omega, SF_2)}, \tag{29}$$

$$S = \sqrt{2S_{ij}S_{ij}}, S_{ij} = \frac{1}{2}\left(\frac{\partial U_i}{\partial x_j} + \frac{\partial U_j}{\partial x_i}\right), \tag{30}$$

$$\sigma_k = 0.176F_1 + 1, \alpha = \frac{26F_1}{225} + 0.44, \beta = 0.0828 - 0.0078F_1, \sigma_\omega = \frac{89F_1}{107} + \frac{125}{107}, \tag{31}$$

$$f_r = \max\left[\min\left(\frac{4\cdot r'}{1 + r'}\left(1 - tan^{-1}(2r^*)\right) - 1, 1.25\right), 0\right], \tag{32}$$

where U_i is the averaged velocity component, S is the magnitude of the strain rate tensor (S_{ij}), functions r' and r^* depend on combinations of strain rate and vorticity tensors, and F_1 and F_2 are the blending functions. Their formulation is based on the distance to the nearest surface and the flow variables. Various coefficients in Formula (31) are empirical and change their value depending on the value of the blending functions. It is necessary to take into account the empirical function fr increasing turbulence of the flow due to rotation, proposed by the authors from [13,14]. It is a multiplier of the production term P_k in Formula (28). The specific limiter 1.25 provided a good compromise for different test cases that have been considered with the SST model (for example, flow through a U-turn, flow in a hydro cyclone, and flow over a NACA 0012 wing tip vortex [14]).

When studying heat transfer using the ORS turbulence model, the mathematical formulation becomes more complicated [12] since, firstly, the momentum (33) and ω (34)–(36) transfer equations are changed, and secondly, six additional turbulent stress transfer equations are added to the system (37)–(40):

$$\frac{\partial(\rho U_i)}{\partial t} + \frac{\partial(\rho U_i U_j)}{\partial x_j} - \frac{\partial}{\partial x_j}\left(\mu\left(\frac{\partial U_i}{\partial x_j} + \frac{\partial U_j}{\partial x_i}\right)\right) = -\frac{\partial}{\partial x_i}\left(P + \frac{2}{3}\mu\frac{\partial U_k}{\partial x_k}\right) - \frac{\partial\left(\rho\overline{u_i u_j}\right)}{\partial x_j}, \tag{33}$$

$$\frac{\partial(\rho\omega)}{\partial t} + \frac{\partial(\rho U_k\omega)}{\partial x_k} = \frac{5}{9}\frac{\rho\omega}{k}P_k - 0.075\rho\omega^2 + \frac{\partial}{\partial x_k}\left(\left(\mu + \frac{\mu_t}{2}\right)\frac{\partial\omega}{\partial x_k}\right), \tag{34}$$

$$P_k = \mu_t \left(\frac{\partial U_i}{\partial x_j} + \frac{\partial U_j}{\partial x_i} \right) \frac{\partial U_i}{\partial x_j} - \frac{2}{3} \frac{\partial U_k}{\partial x_k} \left(3\mu_t \frac{\partial U_k}{\partial x_k} + \rho k \right), \quad (35)$$

$$\mu_t = \rho \frac{k}{\omega} = \frac{\rho}{2\omega} (\overline{u_l u_l}), \quad (36)$$

$$\frac{\partial (\rho \overline{u_i u_j})}{\partial t} + \frac{\partial (U_k \rho \overline{u_i u_j})}{\partial x_k} = P_{ij} - 0.06 \rho \omega k \delta_{ij} + \phi_{ij} + \frac{\partial}{\partial x_k} \left(\left(\mu + \frac{\mu_t}{2} \right) \frac{\partial \overline{u_i u_j}}{\partial x_k} \right), \quad (37)$$

$$P_{ij} = -\rho \overline{u_i u_k} \frac{\partial U_j}{\partial x_k} - \rho \overline{u_j u_k} \frac{\partial U_i}{\partial x_k}, P = 0.5 P_{kk}, \quad (38)$$

$$\phi_{ij} = 0.162 \rho \omega \left(\frac{2}{3} k \delta_{ij} - \overline{u_i u_j} \right) - \frac{213}{275} \left(P_{ij} - \frac{2}{3} P \delta_{ij} \right) - \frac{54}{275} \left(D_{ij} - \frac{2}{3} P \delta_{ij} \right) - \frac{136}{275} \rho k \left(S_{ij} - \frac{1}{3} S_{kk} \delta_{ij} \right), \quad (39)$$

$$D_{ij} = -\rho \overline{u_i u_k} \frac{\partial U_k}{\partial x_j} - \rho \overline{u_j u_k} \frac{\partial U_k}{\partial x_i}, \quad (40)$$

where u_i is the fluctuating component of the velocity, P_{ij} is the production tensor of Reynolds stresses, ϕ_{ij} is the pressure–strain correlation, and D_{ij} is the tensor from the pressure–strain model. The buoyancy effects on turbulence were not taken into account according to the recommendation from [12] because the ratio of the Grashof and Reynolds numbers at the lowest flow rate is $Gr/Re^2 < 1$. At the wall region, demonstrated in the motion and heat transfer modeling, the unified wall law according to B.A. Kader was used [29]. The wall temperature at the liquid–wall boundary was determined from the condition of heat fluxes' equality.

The calculation was carried out in a stationary formulation with a timescale (time step) equivalent to the Courant number within the 30–50 range. The simulation stopped when the following conditions were met simultaneously: the RMS of the residuals was less than $10^{-4,}$ and imbalances of velocity components, mass flow, and heat flux for the mesh regions were less than 10^{-3}. CFX's solver uses an element-based finite volume method. The mesh is used to construct finite volumes, which are used to conserve relevant quantities such as mass, momentum, and energy. The equations for mass, momentum, and a passive scalar are integrated over each control volume. The advection scheme is high resolution (HRS) [12]. It is based on a first-order upwind difference scheme (UDS), but HRS uses a special nonlinear recipe for the specified blend factor (β) at each node, computed to be as close to 1 as possible. The equality β to 1 formally leads to second-order accuracy in space, and the resulting discretization will more accurately reproduce steep spatial gradients than the first-order UDS. The tri-linear shape functions are used to evaluate spatial derivatives for all the diffusion terms of the finite-element model part [12]. The summation is carried out over all the shape functions for the element. The Cartesian derivatives of the shape functions are expressed in terms of their local derivatives. The shape function gradients are evaluated at the actual location of each integration point.

Boundary conditions for the full grid model of each intensifier were various combinations of the first and second circuits' mass flow rates and input temperatures (Table 2). The fluids' movement and gravity action directions are shown in Figure 8a. Outlet pressure for each circuit was set equal to 0. The channels' sidewalls had no slipping. The operating water pressure was in accordance with the experimental values. There were no heat losses in any direction. Temperature dependence of water's physical properties was taken into account.

Table 2. The regime's parameters for heat transfer study.

Circuit	Parameter	Regimes				
I	G_1 (kg/h)/T_{in1} (°C)	11/245	46/250	71/255	184/255	277/260
II	G_2 (kg/h)/T_{in2} (°C)	4/35	19/36	38/38	76/42	114/50

The boundary condition for the isothermal swirling-flow study was the mass flow rate in the range of 8–80 kg/h. Gravity force was not taken into account (Figure 8b). The pressure at the outlet was 0. The operating pressure of water was 1 atm. The channel sidewall had no slipping. Water's physical properties were taken at 20 °C. For all numerical studies in the inlet boundaries, the ratio of the root mean square of velocity fluctuations (u) and the mean flow velocity (U), named turbulence intensity, is equal to 0.05.

The grid independence study was based on a comparison of heat transfer coefficient averaged values and the tangential velocity profiles determined. The elements' number and thickness growth coefficient in the wall region varied in the channel cross-section (Figure 9a,c,e). For each cross-section version, three grid linear density variants were considered (Figure 9b,d,f). Nine grid model variants were studied in total.

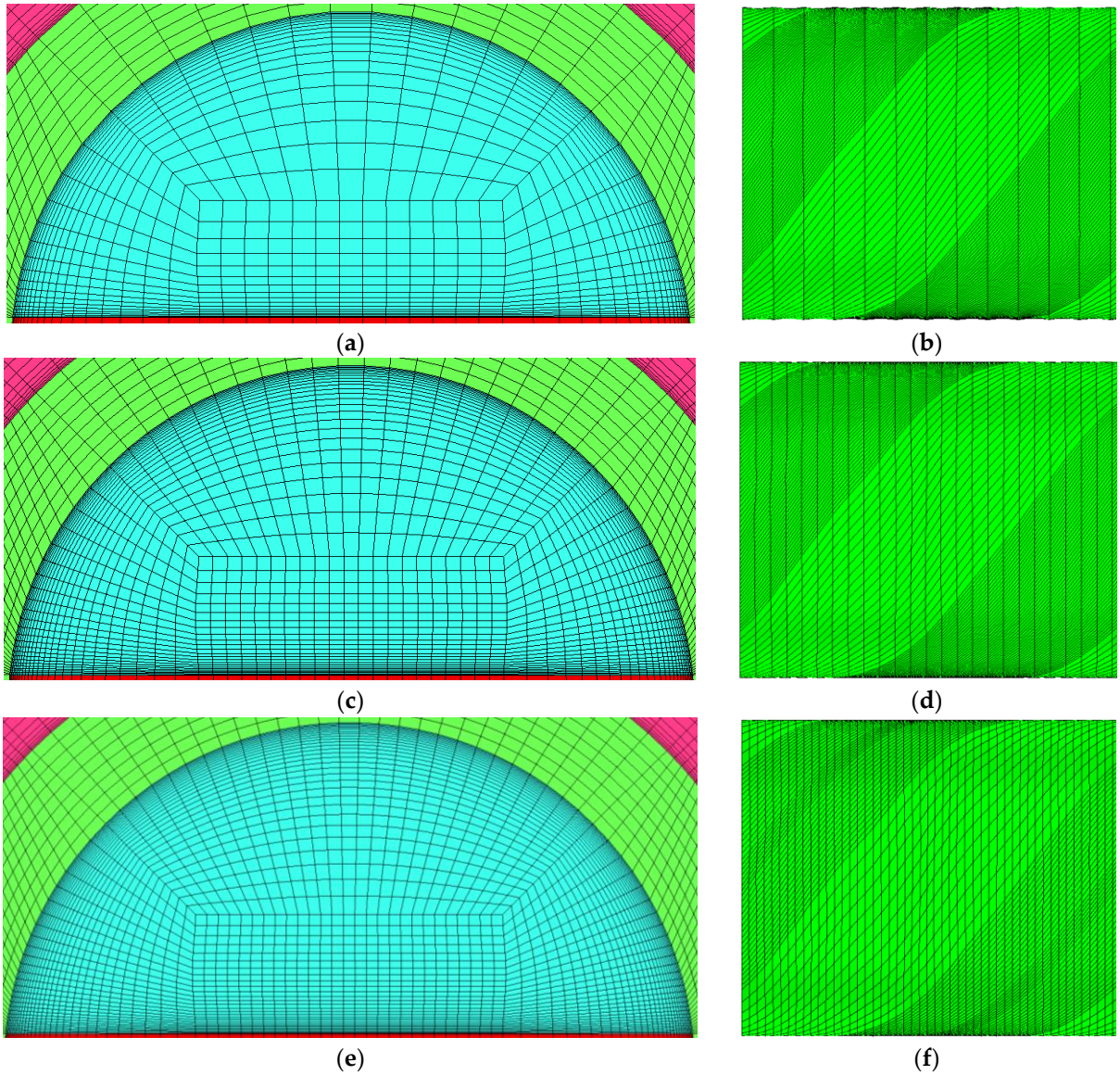


Figure 9. General view of grids for one twist step: (**a**) section type 1 (S1); (**b**) length type 1 (L1); (**c**) section type 2 (S2); (**d**) length type 2 (L2); (**e**) section type 3 (S3); (**f**) length type 3 (L3).

All meshes consist of hexahedral elements adapted to the swirling streamline orientations. The finite element and volumetric mesh models were connected "node to node". The total elements' numbers for each type of grid are given in Table 3. The most heat-stressed

heat exchanger state (G_1/G_2 = 277/144) with the s/d = 2 intensifier was modeled. The simulations using SST and ORS turbulence models were performed.

Table 3. Elements' numbers for different grid types.

Grid Section Type	L1	L2	L3
S1	17×10^6	33×10^6	66×10^6
S2	26×10^6	50×10^6	99×10^6
S3	33×10^6	66×10^6	123×10^6

Figure 10 shows the dependence of the ratio's average numerical Nu value on its experimental value for grids of different types and dimensions.

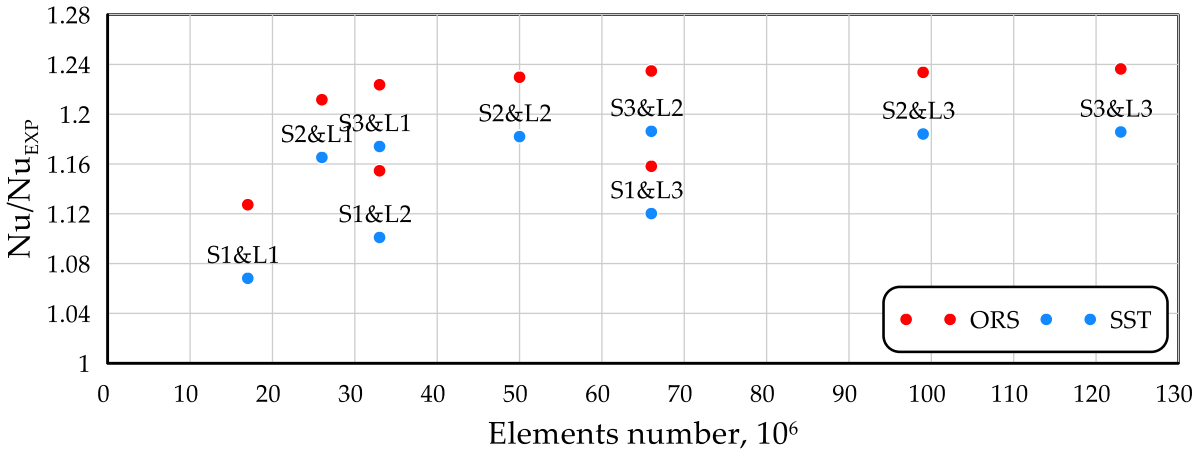


Figure 10. Heat transfer coefficient averaged values.

The grid model's low density in the section did not allow correct modeling of the velocity field (Figure 11). Comparing the tangential velocity component radial distributions, it can be noted that a thickness growth coefficient higher than 1.2 should be avoided, as well as not allowing a significant excess of the longitudinal elements' size of the transverse ones.

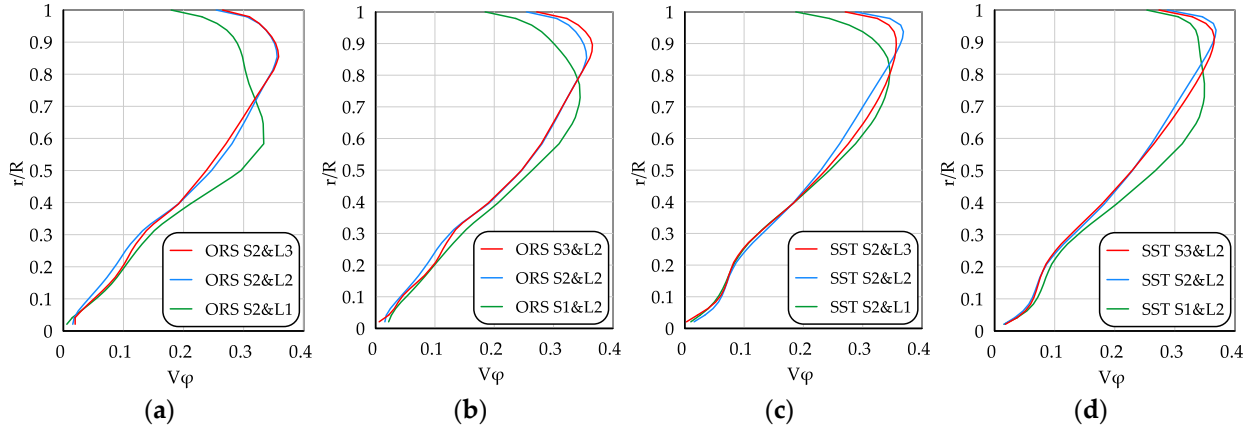


Figure 11. Tangential velocity profile from grid independence study: grid linear density variations with ORS (**a**) and SST (**b**) models; grid surface density variations with ORS (**c**) and SST (**d**) models.

As a result, the mesh type S2&L2 was selected (Figure 12). Other twisting steps models had similar settings. Grids with tetrahedral elements were not considered because these elements' normal vectors are not oriented along the swirling streamlines. This may lead to a numerical diffusion significant influence on the results in a long channel.

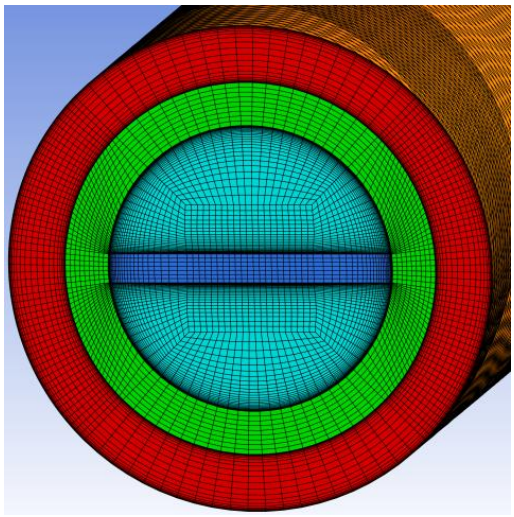


Figure 12. General view of selected type of mesh (S2&L2).

6. Numerical Data Processing

By analogy with experimental modes, the main aim of the numerical temperature field analysis was to determine the heat transfer coefficient distributions. Chaotically occurring zones of temperature gradients in the wall region were discovered (Figure 13a). It was necessary to determine the local heat transfer coefficient values in several directions. To solve this problem, a set of cross-sections was built according to the model height—one-by-one flow step rotation through 90°. Three main directions (Roman numerals) of heat transfer were identified (Figure 13b).

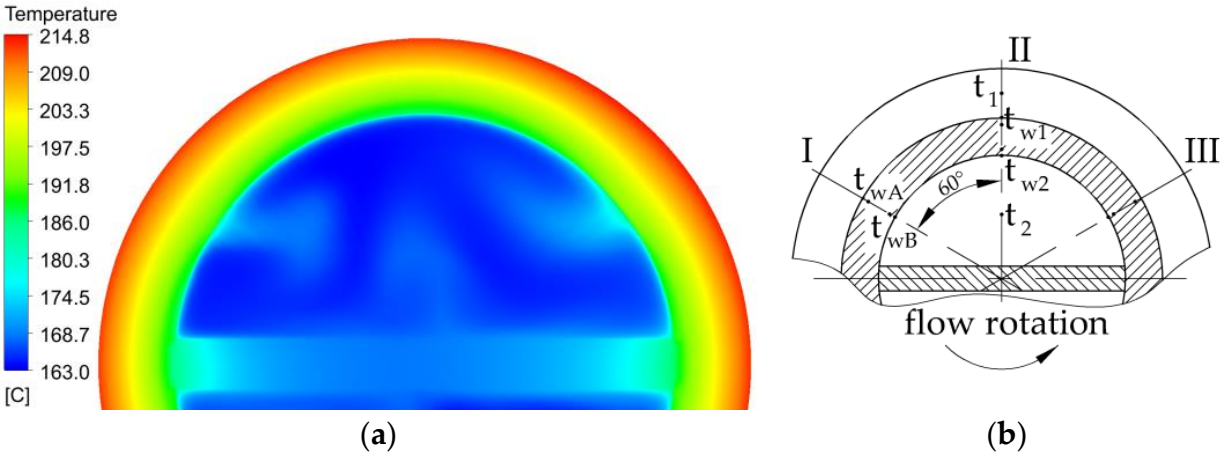


Figure 13. Processing of numerical data: (**a**) instantaneous temperature field in a random cross-section; (**b**) schematic view of temperature control points.

Each section has the following temperature control points:

- Heating coolant temperature: one (T_1) for the center and one (T_{W1}) for inside the wall region (center of first wall element);
- Three sets of T_{WA}, T_{WB} (1 mm distance) for metal temperature control and the linear thermal flux density (q_l) calculation:

$$q_l = \frac{Q}{l} = \frac{2\pi\lambda_{metal}}{\ln(r_{TwA}/r_{TwB})}(t_{wA} - t_{wB}) = \frac{2\pi\lambda_{metal}}{0.175}(t_{wA} - t_{wB}); \quad (41)$$

- Three T_{W2} in the wall region of heated flow (center of first wall element) for the heat transfer coefficient calculation (α) for each direction:

$$\alpha = \frac{q_l}{(\pi d - 2\delta)(t_{w2} - t_2)} = \frac{q_l \cdot 10^3}{2.94(t_{w2} - t_2)}; \quad (42)$$

- Heated coolant temperature (T_2).

An example of the local heat transfer coefficients' distribution along the model length is shown in Figure 14. The outer (I), middle (II), and inner (III) flow zones are characterized by a different velocity profile and flow turbulence intensity. The distribution analysis confirmed the absence of spatial regularity of temperature gradient regions' occurrence in the wall region. A more detailed spectral distribution analysis was not carried out since this requires additional correct velocity and temperature field modeling: at the least, nonstationary LES formulation with the Courant number < 1. At the stage of final comparison with the experiment, the value of α was averaged (α_c):

$$\alpha_c = \frac{\alpha_I + \alpha_{II} + \alpha_{III}}{3}. \quad (43)$$

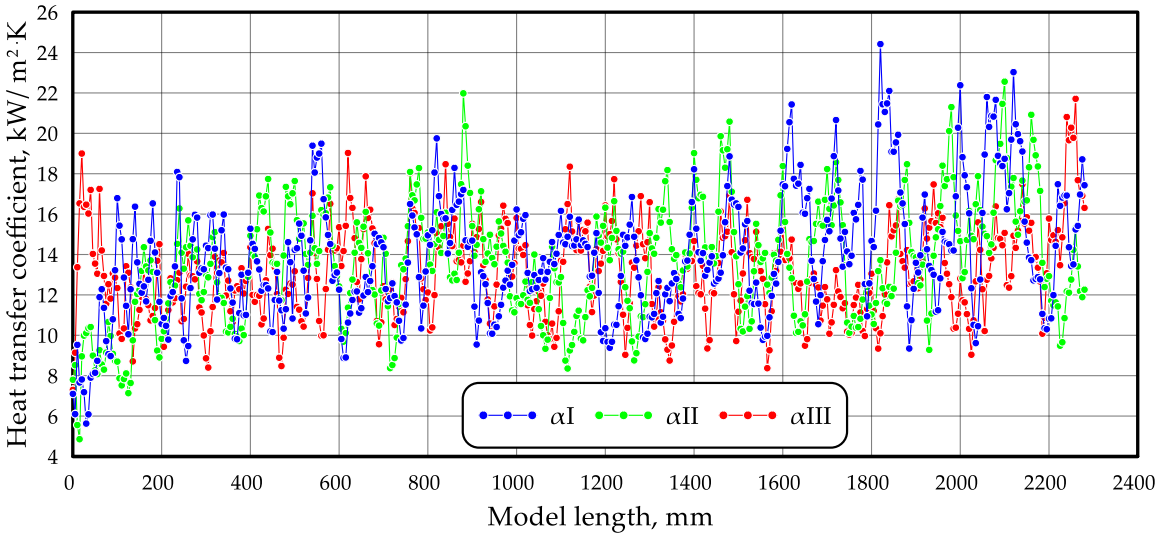


Figure 14. Local heat transfer coefficients' distribution along the model length for intensifier s/d = 2 at G_1/G_2 = 277/114.

7. Results

The friction factor at T = const with swirlers of constant and variable twist pitch is shown in Figure 15.

The experimental values of R.M. Manglik and A.E. Bergles were calculated by dependencies (8). The experimental values of Koch R. were calculated by dependencies (5), which are valid under conditions of laminar motion mode with macro vortices, and the Reynolds critical numbers by (7) (Table 4).

Table 4. The Re critical numbers for intensifiers with const step.

Type of Swirlers	s/d = 2	s/d = 3	s/d = 4
Re_{cr1}	22.4	32.4	42.6
Re_{cr2}	19,710	13,170	10,090

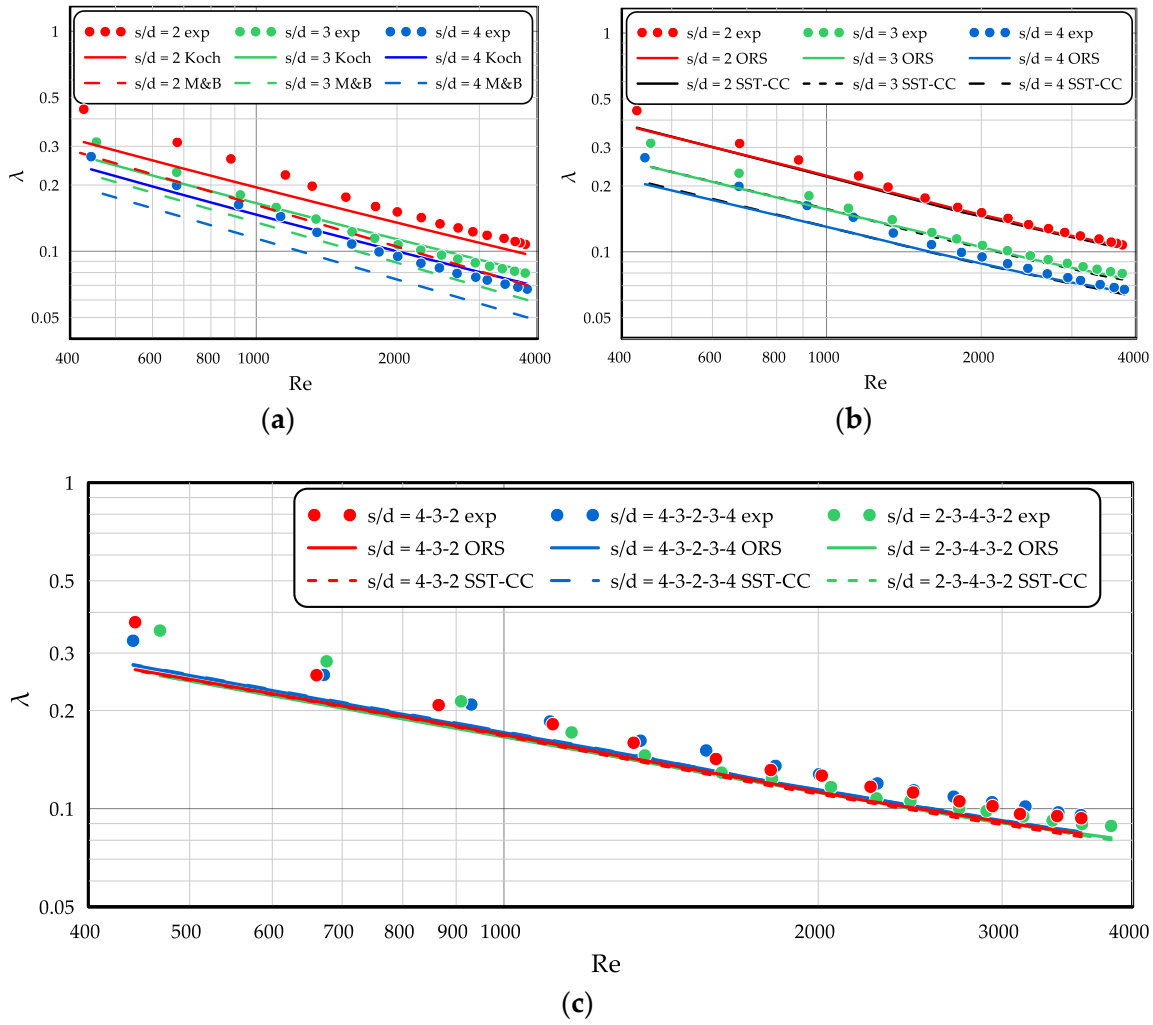


Figure 15. Channels' friction factor at T = const: (**a**) constant twist pitch (only exp); (**b**) constant twist pitch (exp with num); (**c**) variable twist pitch.

The RMS deviation of the experimental values from numerical and generalized dependences, calculated by Formula (44), are shown in Table 5.

$$\sigma_\lambda = \sqrt{\sum_{i=1}^{N} \frac{(\lambda_i - \lambda_{\text{exp}})^2}{N}}. \quad (44)$$

Table 5. RMS experimental values deviation from numerical and generalized dependences.

Type of Swirlers	Koch R.	Manglik and Bergles	ORS	SST-CC
s/d = 2	0.0416	0.1162	0.0265	0.0261
s/d = 3	0.0153	0.0671	0.0234	0.0235
s/d = 4	0.0211	0.0551	0.0361	0.0351
s/d = 4-3-2	-	-	0.0398	0.0398
s/d = 4-3-2-3-4	-	-	0.0243	0.0237
s/d = 2-3-4-3-2	-	-	0.0349	0.0349

The calculated values are slightly lower than the experimental ones because of the high idealization degree of the geometric model. Swirlers consist of separate fragments connected by spot welding, which cannot ensure complete side surfaces' docking of the connected parts. Variable pitch swirlers have additional such connections. The numerical

values (ORS and SST-CC) of pressure drops in the presence of heat exchange differ by less than 1%. More complex experimental study conditions, associated first of all with a large number of inaccuracies in the inner channel geometric shape, cause significant differences from the generalized dependencies obtained at an atmosphere or low gauge pressure.

The heat exchanger temperature conditions can be divided into three groups:

- The mode of fast swirled-flow warm-up at $G_1/G_2 > 2$ (Figure 16a);
- The mode with an optimal flow ratio at $2 > G_1/G_2 > 0.5$ (Figure 16b);
- The mode of slow swirled-flow warm-up at $0.5 > G_1/G_2$ (Figure 16c).

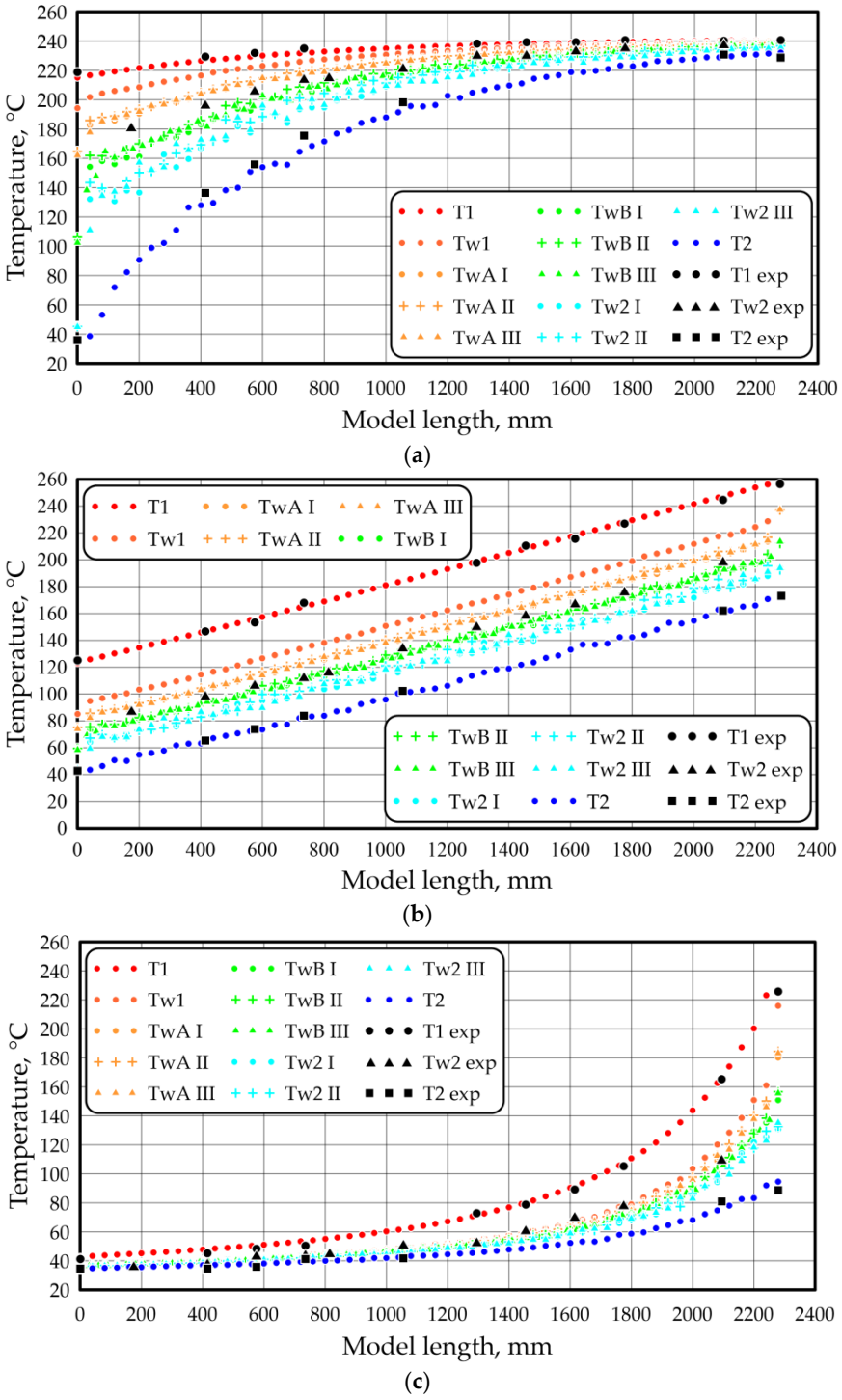


Figure 16. Temperature fields (ORS and exp): (**a**) $G_1/G_2 > 2$; (**b**) $2 > G_1/G_2 > 0.5$; and (**c**) $0.5 > G_1/G_2$.

The small deviations in the calculated values from the general trend are explained by the local heat transfer peculiarities due to the vortex structure generation, the thermogravitation effect, and the intensifier heat conduction influence.

The RMS deviations between numerical and experimental temperature data's overall flow rates range, calculated using a formula similar to 44, are given in Table 6.

Table 6. RMS deviations between the numerical and experimental temperature data (°C).

Type of Swirlers	ORS (T_{F2})	SST-CC (T_{F2})	ORS (T_{W2})	SST-CC (T_{W2})
s/d = 2	6.4	6.4	11.3	11.5
s/d = 3	6.4	6.5	10.9	11.0
s/d = 4	6.3	6.4	11.4	11.2
s/d = 4-3-2	5.9	6.0	10.8	10.7
s/d = 4-3-2-3-4	5.9	5.9	10.7	10.8
s/d = 2-3-4-3-2	5.8	5.9	10.9	10.9

It is possible to note a worse coincidence of temperature fields with a significant difference between coolant flow rates. Significant axial temperature gradients are more difficult to localize. Using a larger number of thermocouples for the swirling flow temperature would reduce the error. Significant errors in the wall temperature can be associated with a large logarithmic mean temperature difference between the flows and a greater inaccuracy in the spatial arrangement of the experimental thermocouples. Obtaining a complete match of temperature fields is impossible due to the high level of numerical model idealization.

A more correct approach is to compare the average values of the heat transfer coefficients. The experimental Nu (Re) obtained for the intensifiers with a constant swirl pitch with an almost uniform temperature difference along the model length are shown in Figure 17. The heat flux constancy condition along the channel length allows us to make a comparison with the results of semi-empirical formulas. During the swirling flow heating, a significant change in the Prandtl number occurs. This leads to several values of Nusselt number presence at the same Reynolds number. The RMS deviations between the experimental and semi-empirical Nu for modes with an optimal flow ratio, calculated using a formula similar to 44, are given in Table 7. There is good agreement between all experimental data on heat transfer.

Table 7. RMS deviations between experimental and semi-empirical Nu.

Type of Swirlers	Koch R.	Manglik & Bergles
s/d = 2	4.70	5.91
s/d = 3	5.28	4.96
s/d = 4	4.64	6.97

The thermal efficiency of variable pitch intensifiers application can be estimated based on total thermal load (45) comparison for G_1/G_2 = 277/114. The values are given in Table 8.

$$Q_{tot} = G_2(H_{out} - H_{in}), \quad (45)$$

where H_{in} and H_{out} are the secondary circuit enthalpies at the inlet and outlet of the model.

Analyzing this table, it is important to take into account the non-complete coincidence of the operating parameters during experimental studies. A small discrepancy between the inlet temperatures and coolant flow rates can cause up to 5% changes in the values presented in the table. Larger values of heat loads for the numerical calculations can be explained by the heat loss' complete absence in all directions. For the overwhelming quantity of modes, it can be noted that both numerical approaches lead to almost identical values of Q. The thermal load difference between the tapes is explained by the fragment s/d = 2 different lengths since it provides the highest local heat transfer coefficients.

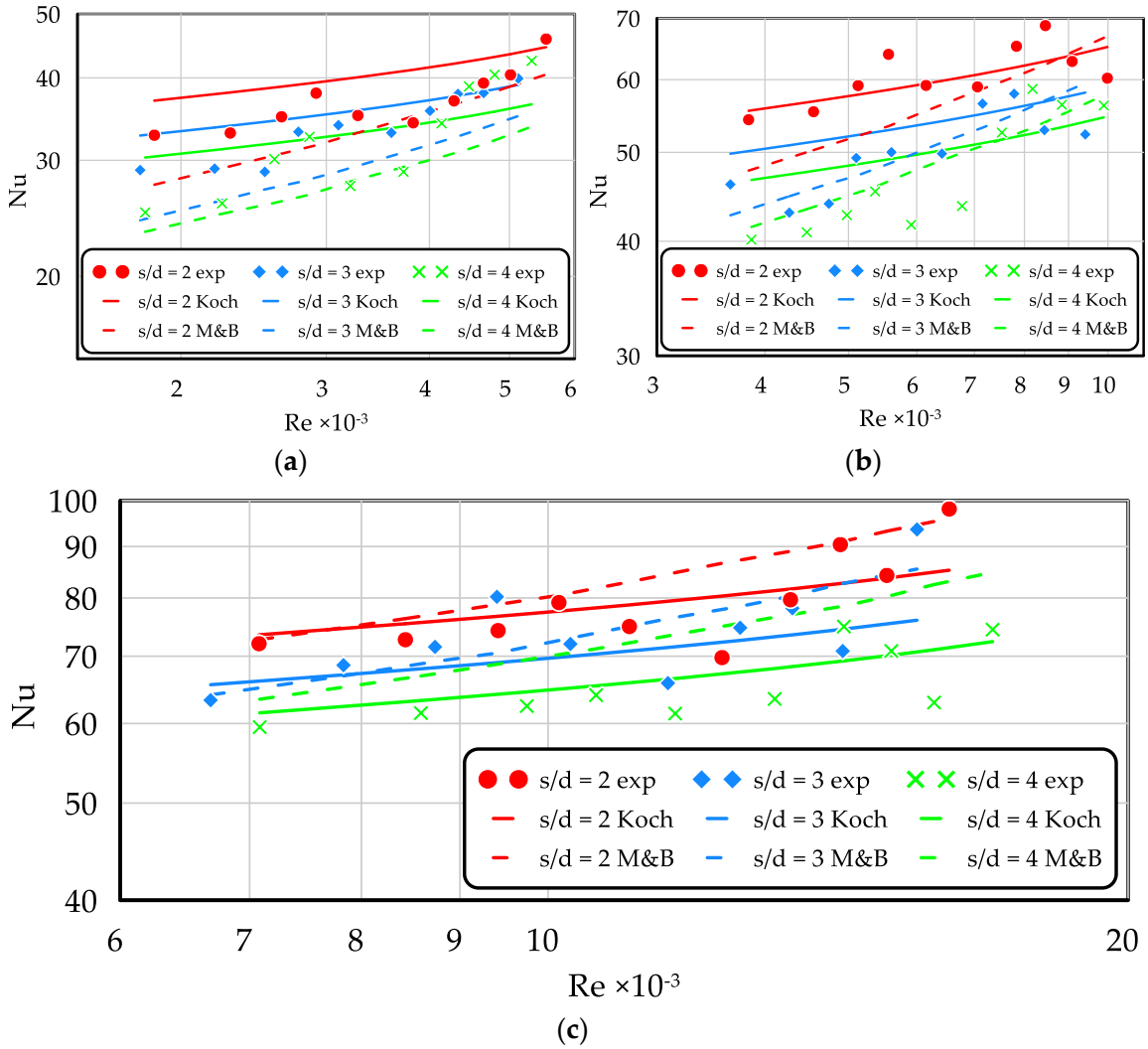
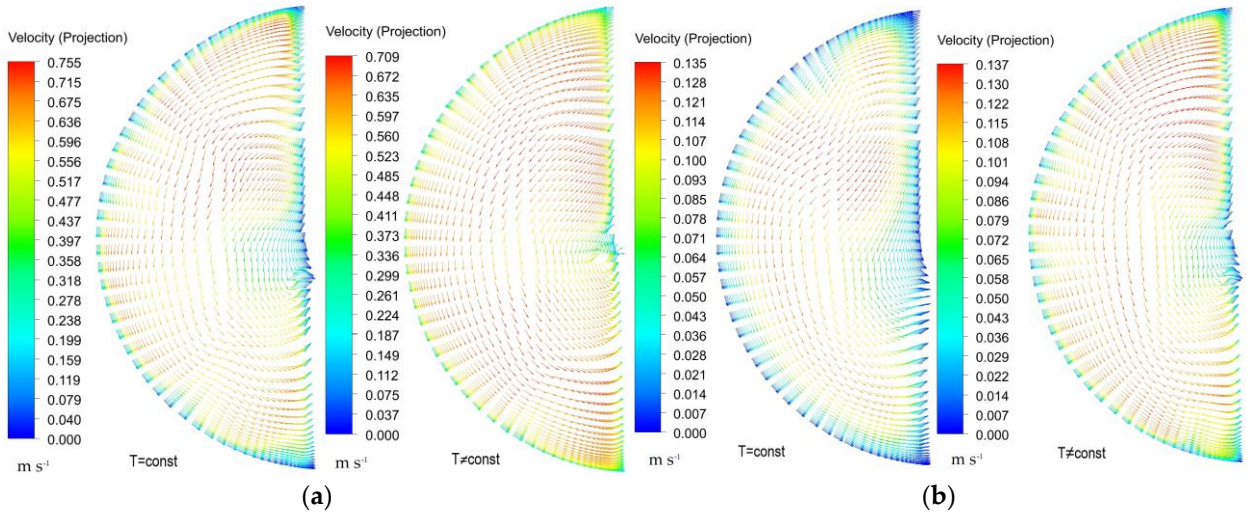


Figure 17. The *Nu* = *f*(*Re*): (**a**) G_1/G_2 = 46/38; (**b**) G_1/G_2 = 71/76; and (**c**) G_1/G_2 = 184/114.

Table 8. Total thermal load (W) at maximum coolant flow rates.

Type of Swirlers	Exp	ORS	SST-CC
s/*d* = 2	21,100	21,520	21,519
s/*d* = 3	20,370	20,872	20,870
s/*d* = 4	19,760	20,145	20,143
s/*d* = 4-3-2	20,060	20,391	20,389
s/*d* = 4-3-2-3-4	20,490	20,920	20,919
s/*d* = 2-3-4-3-2	19,420	19,823	19,821

Numerical models allow us to conduct a more detailed swirling flow structure analysis. Some flow features, such as local hydrodynamic or temperature effects, can be identified. A velocity fields comparative analysis for thermal and isothermal states revealed several features: at high Reynolds values in the presence of heating, due to a decrease in viscosity, the flow detachment zone in the central part of the channel occurs much earlier (Figure 18a); at low Reynolds numbers, the temperature gradient in the wall region leads to the zone's appearance, mentioned earlier (Figure 18b). These effects are more clearly visible in the fields obtained using the ORS turbulence model. It is important to note the high qualitative coincidence level of the axial velocity component fields, calculated by both models and the experimental values obtained in air [19,21] (Figure 19).



(**a**) (**b**)

Figure 18. Velocity fields (ORS model): (**a**) *Re* = 3900 and (**b**) *Re* = 650.

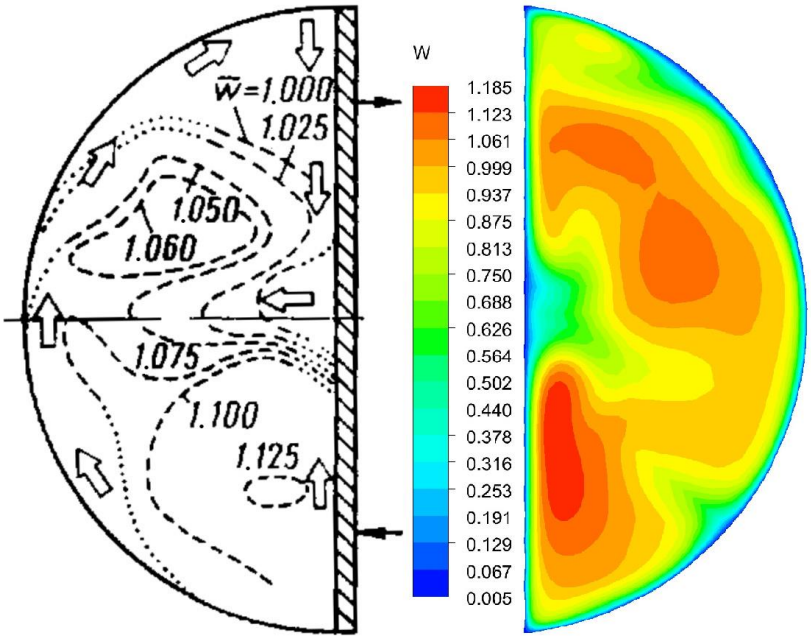


Figure 19. Axial velocity component fields: experimental (**left**); calculated (**right**).

Vector fields of the velocity tangential component for both models confirm the presence of two vortex regions rotating in the same direction (Figure 20a,b). Such vortex structures arise not only in the model's initial section but in other sections and at different flow rates. The tangential velocity field in model outlet section is also similar for both models (Figure 20c,d). Only a small difference can be seen in the near-wall region. It is associated with the local velocity gradients' occurrence due to the temperature gradient. The spatial zone distribution depends on the time step (the iteration number for quasi-statical calculations) and radial velocity distribution. Figure 21 shows the process of tangential velocity field evolution. It can be noted that the radius corresponding to the maximum tangential velocity for the SST model is always larger, i.e., most of the flow has rotation according to the rigid body law.

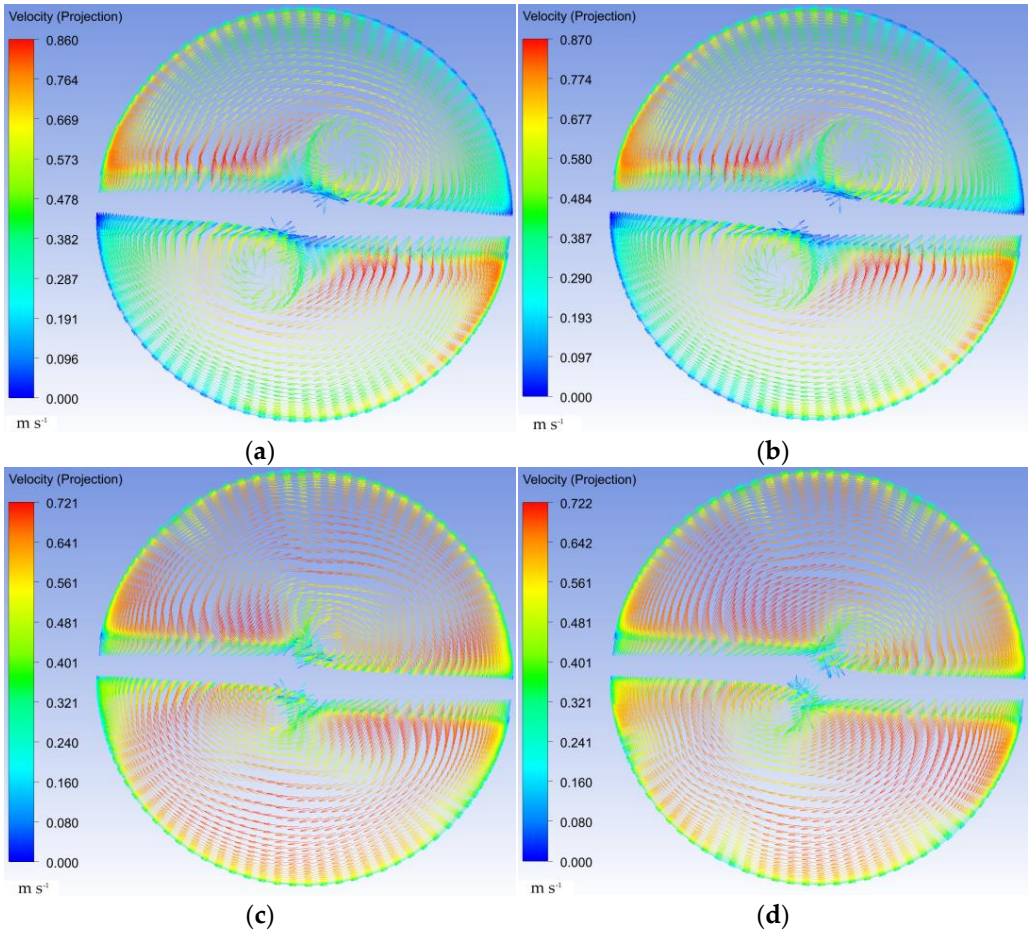


Figure 20. Tangential velocity component fields at G_1/G_2 = 277/144 after 180° flow turn: (**a**) ORS; (**b**) SST-CC; and in model outlet section: (**c**) ORS; (**d**) SST-CC.

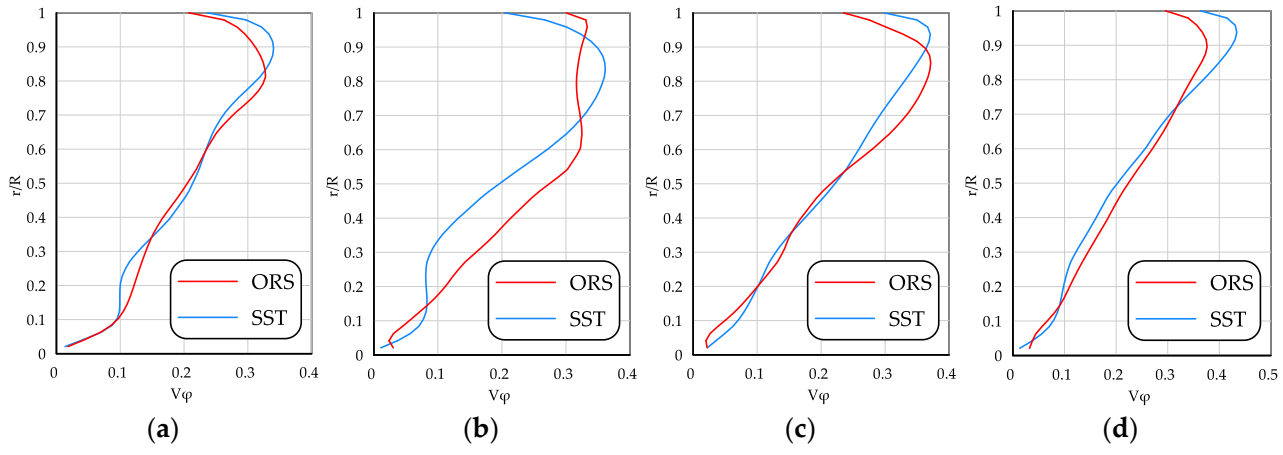


Figure 21. Tangential velocity profile evolution for intensifier s/d = 2 at G_1/G_2 = 184/144: (**a**) l = 4s; (**b**) l = 44s; (**c**) l = 72s; and (**d**) l = 96s.

For variable pitch intensifiers, the most interesting point is how the flow responds to twist pitch changes. The example of a step transition from s/d = 3 to 2 (Figure 22) shows that after two full turns (2 × 360°) of the flow, the velocity profile on the ORS model has been restored, while on the SST model, it has not.

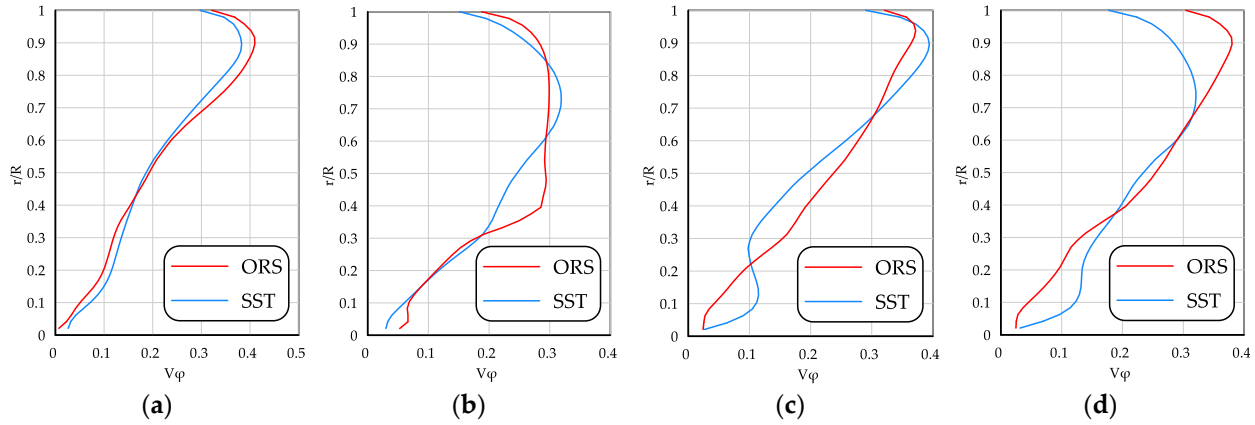


Figure 22. Tangential velocity profile evolution for intensifier *s*/*d* = 4-3-2 at G_1/G_2 = 184/144: (**a**) one step before change *s*/*d* = 3 to 2; (**b**) change section; (**c**) 360° after; and (**d**) 720° after.

The study of local heat transfer effects includes a comparative analysis of heat transfer coefficient distributions along the model length. When the flow rate of the heating coolant exceeds the flow rate of the heated coolant by more than two times, a heat exchange 'acceleration' on the initial section occurs, followed by a low-intensity process of heat transfer. With the opposite ratio, the heat flow from the first circuit is too low to obtain high values for the heat transfer coefficient.

The states with ratio G_1/G_2 = 184/114 = 1.61 are of greatest interest (Figure 23).

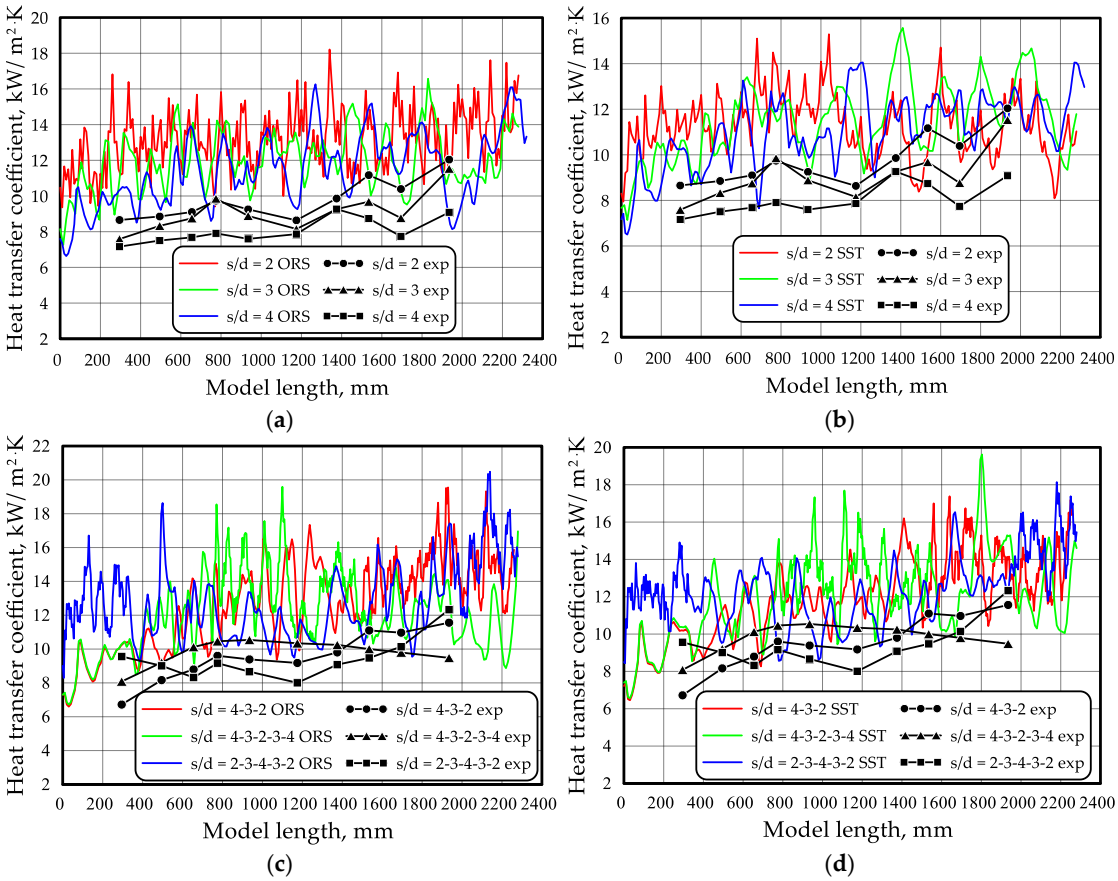


Figure 23. Heat transfer coefficient distributions at G_1/G_2 = 184/114: (**a**,**b**) constant twist pitch; (**c**,**d**) variable twist pitch.

A higher level of temperature field details in the calculation allows us to estimate the contribution of the changing twist pitch to the heat transfer process. Each step pitch corresponds to a specific level of heat transfer coefficient value. This observation is also true for variable pitch intensifiers. In sections with a 20 mm step, there is an increase in the heat transfer coefficient by 1.2–1.4 times compared to a step equal to 40 mm. Periodic spikes of the heat transfer coefficient value are explained by the control point hit in the zones of high-temperature gradients.

Variable twist pitch intensifiers are also more interesting from a numerical modeling point of view. A heat transfer coefficient numerical distributions comparison (SST-CC and ORS) is shown in Figure 24:

- The qualitative and quantitative coincidence of distributions in the initial fragment (flow stabilization);
- The heat transfer coefficient value (averaged by length) for the SST model is 5% less;
- Smaller values of heat transfer coefficient gradients arise when the twist pitch changes in the SST model.

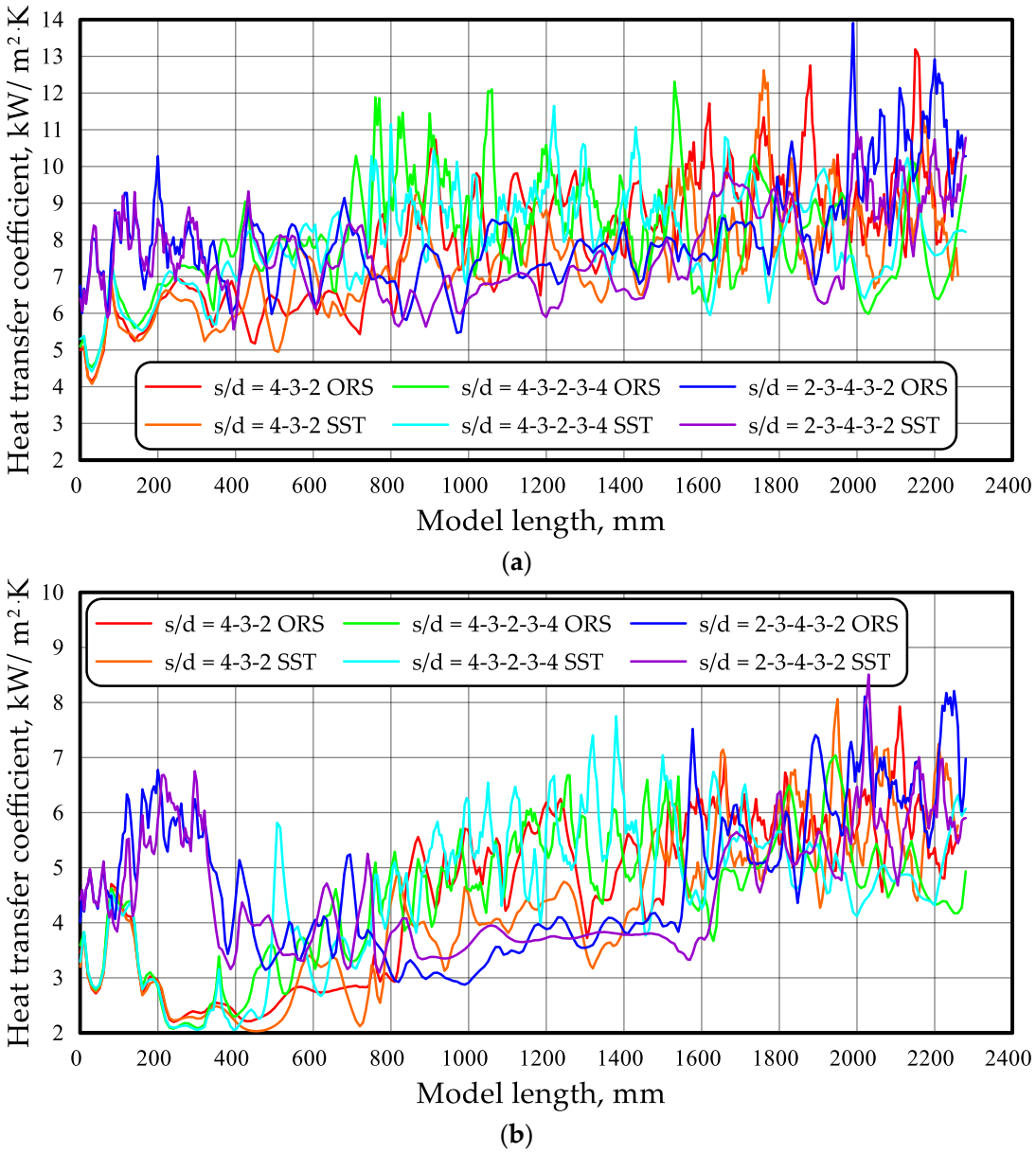


Figure 24. Heat transfer coefficient distributions: (**a**) G_1/G_2 = 71/76 and (**b**) G_1/G_2 = 184/38.

A high value of average heat transfer coefficient is maintained by the presence of twist pitch of 20 mm fragments. Fragments with a larger pitch have a lower friction coefficient. In the zones of a twist pitch change, a local heat transfer increase is observed. It is associated with the restructuring of the boundary layer. All these swirling flow movement features lead to a high efficiency of intensifiers with variable twist pitch.

The intensification effectiveness coefficients by tape swirlers were estimated using Formula (46) [30]. The states with the optimal flow rates ratio were processed.

$$k_{eff} = \frac{\alpha_{int}}{\alpha_{tube}} \frac{F_{int}}{F_{tube}} \text{ if } \frac{\Delta P_{int} G_{int}}{\Delta P_{tube} G_{tube}} \approx 1. \quad (46)$$

where F is the heat exchange surface area, ΔP is the channel pressure drop, G is the mass flow rate, α is the heat transfer coefficient, and the *int* and *tube* indexes indicate that the value belongs to a channel with and without an intensifier. The calculation results, based on experimental data, are presented in Table 9. The experimental temperature and velocity fields for the channel without an intensifier are not included in this article. With a non-optimal flow rates ratio, intensifiers with a variable twist pitch also performed best [15].

Table 9. Intensification effectiveness coefficients.

Type of Swirler	k	Type of Swirler	k
s/d = 4	1.07	s/d = 2-3-4-3-2	1.11
s/d = 3	1.11	s/d = 4-3-2	1.21
s/d = 2	1.14	s/d = 4-3-2-3-4	1.31

8. Conclusions

Variable twist pitch intensifiers provide greater efficiency because they enable high heat transfer coefficients to be achieved at lower hydraulic power consumption for coolant motion. This becomes possible despite a pressure drop increase due to a decrease in the coolant average density (at the same mass flow rate) due to the swirling flow's improved heating compared to a whole pipe. With a significant difference in coolant flow rates in the heat exchanger (not nominal or transition mode), its efficient operation is also ensured.

Using the Omega Reynolds stress turbulence to model the motion and heat transfer computations of swirling flows in complex geometry channels allows us to study the structure of thermal and hydrodynamic boundary layers with sufficient accuracy. The SST model, with a correction for curvature streamlines, allows us to obtain a slightly worse result but in a shorter time: the calculation time is 15–20% lower since many fewer transfer equations are solved. The best results can be achieved by the LES approach to turbulence modeling, but this will significantly increase the calculation time. Comparative analysis of the velocity fields showed a small advantage with the ORS model. This is due to the solution of additional equations for the transfer of turbulent stresses. Experimental values of the heat transfer coefficient are lower than the numerical ones. In many ways, the discrepancies between the calculated and experimental data are due to the complexity of the experiment and the high level of idealization of the calculated model.

Author Contributions: Conceptualization, S.D. and A.K.; data curation, A.S.; formal analysis, A.S.; investigation, S.D., A.K., and A.S.; methodology, S.D. and A.K.; software, A.S.; supervision, S.D.; validation, A.S.; visualization, A.S.; writing—original draft, A.K. and A.S.; writing—review and editing, A.K. and A.S. All authors have read and agreed to the published version of the manuscript.

Funding: This research received no external funding.

Data Availability Statement: The original contributions presented in the study are included in the article, further inquiries can be directed to the corresponding author.

Conflicts of Interest: The authors declare no conflicts of interest.

Nomenclature

ORS	Omega-Based Reynolds Stress Model
SST-CC	Shear Stress Transport Model with Curvative Correction
PWR	Power Water Reactor
NPU	Nuclear Power Unit
WWER	Water–Water Energetic Reactor
CFD	Computational Fluid Dynamics
DNS	Direct Numerical Simulation
RANS	Reynolds-averaged Navier–Stokes
DES	Detached Eddy Simulation
LES	Large Eddy Simulation
RMS	Root Mean Square

References

1. Kalinin, E.K.; Dreitser, G.A.; Kopp, I.Z.; Myakochin, A.S. *Effective Heat Exchange Surfaces*; Energoatomizdat: Moscow, Russia, 1998.
2. Chunchula, R.B.; Santhosh, K.G. CFD Analysis of Heat Transfer Enhancement by Using Passive Technique in Heat Exchanger. *Int. J. Recent Adv. Mech. Eng.* **2015**, *4*, 99–111.
3. Khafaji, H.Q.A.; Abdul Wahhab, H.A.; Alsaedi, S.S.; Al-Maliki, W.A.K.; Alobaid, F.; Epple, B. Thermal Performance Evaluation of a Tubular Heat Exchanger Fitted with Combined Basket–Twisted Tape Inserts. *Appl. Sci.* **2022**, *12*, 4807. [CrossRef]
4. Bhuiya, M.; Roshid, M.; Talukder, M.; Rasul, M.; Das, P. Influence of perforated triple twisted tape on thermal performance characteristics of a tube heat exchanger. *Appl. Therm. Eng.* **2020**, *167*, 114769. [CrossRef]
5. Bhuiya, M.; Azad, A.; Chowdhury, M.; Saha, M. Heat transfer augmentation in a circular tube with perforated double counter-twisted tape inserts. *Int. Commun. Heat Mass Transf.* **2016**, *74*, 18–26. [CrossRef]
6. Bucak, H.; Yılmaz, F. The current state on the thermal performance of twisted tapes: A geometrical categorization approach. *Chem. Eng. Process. Process Intensif.* **2020**, *153*, 107929. [CrossRef]
7. Piriyarungrod, N.; Kumar, M.; Thianpong, C.; Pimsarn, M.; Chuwattanakul, V.; Eiamsaard, S. Intensification of thermo-hydraulic performance in heat exchanger tube inserted with multiple twisted-tapes. *Appl. Therm. Eng.* **2018**, *136*, 516–530. [CrossRef]
8. Khoshvaght-Aliabadi, M.; Feizabadi, A. Performance intensification of tubular heat exchangers using compound twisted-tape and twisted-tube. *Chem. Eng. Process. Process Intensif.* **2020**, *148*, 107799. [CrossRef]
9. Salam, B.; Biswas, S.; Saha, S.; Bhuiya, M.M.K. Heat Transfer Enhancement in a Tube using Rectangular-cut Twisted Tape Insert. *Procedia Eng.* **2013**, *56*, 96–103. [CrossRef]
10. Man, C.; Lv, X.; Hu, J.; Sun, P.; Tang, Y. Experimental study on effect of heat transfer enhancement for single-phase forced convective flow with twisted tape inserts. *Int. J. Heat Mass Transf.* **2017**, *106*, 877–883. [CrossRef]
11. Wagner, W.; Pruß, A. The IAPWS Formulation 1995 for the Thermodynamic Properties of Ordinary Water Substance for General and Scientific Use. *J. Phys. Chem. Ref. Data* **2002**, *31*, 387–535. [CrossRef]
12. Ansys. *Ansys 19.2 Help*; ANSYS Inc.: Canonsburg, PA, USA, 2019.
13. Spalart, P.R.; Shur, M.L. On the Sensitization of Turbulence Models to Rotation and Curvature. *Aerosp. Sci. Technol.* **1997**, *1*, 297–302. [CrossRef]
14. Smirnov, P.E.; Menter, F.R. Sensitization of the SST turbulence model to rotation and curvature by applying the Spalart-Shur correction term. *J. Turbomach.* **2009**, *131*, 041010. [CrossRef]
15. Sobornov, A.E.; Dmitriev, S.M.; Ryazapov, R.R.; Kotin, A.V. Experimental efficiency evaluation of the of various geometry twisted bands for heat transfer intensification in the heat-exchange channels of a nuclear power unit equipment. *J. Phys. Conf. Ser.* **2021**, *2088*, 012046. [CrossRef]
16. Dmitriev, S.M.; Ryazapov, R.R.; Sobornov, A.E.; Dmitriy, V.S. Numerical and Experimental Research of Swirling Flow Heat Transfer in a Pipe with Equally Twisted Metallic Band. In Proceedings of the 9th International Topical Meeting on Nuclear Thermal-Hydraulics, Operation and Safety (NUTHOS-9), Kaohsiung, Taiwan, 9–13 September 2012; 13p.
17. Sobornov, A.E.; Dmitriev, S.M.; Ryazapov, R.R.; Kotin, A.V. Experimental research of heat transfer in a viscous flow in channels with twisted metallic bands different geometry. *Proc. Nizhny Novgorod State Tech. Univ. R.E. Alekseev №* **2013**, *2*, 134–141.
18. Koch, R. *Pressure Loss and Heat Transfer for Turbulent Flow*; No. AEC-TR-3875; Atomic Energy Commission: Washington, DC, USA, 1960.
19. Shchukin, V.K. *Heat Transfer and Hydrodynamics of Internal Flows in the Mass Forces Fields*; Mashinostroenie: Moscow, Russia, 1980; 240p.
20. Manglik, R.M.; Bergles, A.E. Bergles, Swirl flow heat transfer and pressure drop with twisted-tape inserts. *Adv. Heat Transf.* **2003**, *36*, 183–266.
21. Smithberg, E.; Landis, F. Friction and forced convection heat transfer characteristics in tubes with twisted tape swirl generators. *J. Heat Transf.* **1964**, *86*, 39–49. [CrossRef]
22. Ibragimov, M.M.; Nomofelov, E.V.; Subbotin, V.I. Heat transfer and hydraulic resistance with swirl-type motion of liquid in pipes. *Teploencrgetika* **1961**, *8*, 57–60.

23. Senoo, Y.; Nagata, T. Swirl Flow in Long Pipes with Different Roughness. *Bull. JSME* **1972**, *15*, 1514–1521. [CrossRef]
24. Vignat, G.; Durox, D.; Candel, S. The suitability of different swirl number definitions for describing swirl flows: Accurate, common and (over-) simplified formulations. *Prog. Energy Combust. Sci.* **2022**, *89*, 100969. [CrossRef]
25. Cazan, R.; Aidun, C. Analysis of the secondary vortices in rotating Flow induced by a twisted tape inside a pipe. *Sci. Iran.* **2018**, *25*, 3161–3172. [CrossRef]
26. Mills, A.F. *Heat Transfer*, 2nd ed.; Prentice-Hall: Englewood Cliffs, NJ, USA, 1999.
27. Hepbasli, A.; Biyik, E.; Ekren, O.; Gunerhan, H.; Araz, M. A key review of wastewater source heat pump (WWSHP) systems. *Energy Convers. Manag.* **2014**, *88*, 700–722. [CrossRef]
28. Lushchik, V.G.; Makarova, M.S. Turbulent Prandtl number in the boundary layer on a plate: Effect of the molecular Prandtl number, injection (suction) and longitudinal pressure gradient. *Thermophys. Aeromech.* **2018**, *25*, 169–182. [CrossRef]
29. Kader, B.A. Temperature and concentration profiles in fully turbulent boundary layers. *Int. J. Heat Mass Transf.* **1981**, *24*, 1541–1544. [CrossRef]
30. Gukhman, A.A. Intensification of convective heat transfer and the comparative evaluation problem for heat exchange surfaces. *Therm. Eng.* **1977**, *4*, 5–8.

Disclaimer/Publisher's Note: The statements, opinions and data contained in all publications are solely those of the individual author(s) and contributor(s) and not of MDPI and/or the editor(s). MDPI and/or the editor(s) disclaim responsibility for any injury to people or property resulting from any ideas, methods, instructions or products referred to in the content.